A conservative method for numerical solution of the population balance equation, and application to soot formation

Anxiong Liu[1] and Stelios Rigopoulos[1,*]

[1]*Department of Mechanical Engineering, Imperial College London, Exhibition Road, London SW7 2AZ, UK*

[*]*Corresponding author: Stelios Rigopoulos, s.rigopoulos@imperial.ac.uk*

Abstract

The objective of this paper is to present a finite volume method for the discretisation of the population balance equation with coagulation, growth and nucleation that combines: a) accurate prediction of the distribution with a small number of sections, b) conservation of the first moment (or any other single moment) in a coagulation process, c) applicability to an arbitrary non-uniform grid, and d) speed and robustness that make it suitable for combining with a CFD code for solving problems such as soot formation in flames. The conservation of the first moment of a distribution with respect to particle volume is of particular importance for two reasons: it is an invariant during a coagulation process and it represents conservation of mass. The method is based on a geometric evaluation of the double integrals arising from the finite volume discretisation of the coagulation terms and an exact balance of coagulation source and sink terms to ensure moment conservation. Extensive testing is performed by comparison with analytical solutions and direct numerical solutions of the discrete PBE for both theoretical and physically important coagulation kernels. Finally, the method is applied to the simulation of a laminar co-flow diffusion sooting flame, in order to assess its potential for coupling with CFD, chemical kinetics, transport and radiation models. The results show that accurate solutions can be obtained with a small number of sections, and that the PBE solution requires less than one fourth of the time of the complete simulation, only half of which is spent on the discretisation (the remaining being for the evaluation of the temperature dependence of the coagulation kernel).

1 Introduction

The Population Balance Equation (PBE) is of central importance to the dynamics of polydispersed aerosol systems. It describes the evolution of the distribution of particles in terms of one or more properties, the most important of which is usually a measure of particle size. General reviews of the PBE can be found in [10, 64, 14, 45], while [47] focusses on its coupling with reacting flows.

The PBE is important for the modelling of soot formation for two main reasons. Firstly, the rates of surface processes such as growth and oxidation depend on the surface area and hence on the particle size distribution, while the aggregation rate is also size-dependent. Therefore, knowledge of the distribution is important for the correct modelling of soot formation, even in cases where the prediction of integral properties only (such as soot volume fraction) is required. Secondly, new and more stringent regulations on particulate emissions limit the number of smaller particles being emitted, as they are more harmful for human health, and not just the total mass. Prediction of the particle size distribution can thus aid in the improved design of equipment that meets these aims.

The PBE can be formulated in a discrete or a continuous form. The discrete form was developed first [60] and is a system of ODEs describing the temporal evolution of the number of particles of every possible size.

The range of particle sizes is usually enormous - e.g. for particles ranging from 1 nm - 1 μm in diameter, 10^9 units must be accounted for - and therefore its numerical solution is too expensive for practical problems. The problem is aggravated when the PBE must be coupled with fluid dynamics and the distribution is spatially dependent. Furthermore, surface processes such as growth and oxidation involve the addition or removal of units as small as a single atom, which must therefore be the smallest unit in a discrete PBE featuring such processes. These considerations lead to the formulation of a continuous PBE.

The continuous PBE is a single integro-partial differential equation whose derivation has been discussed in a number of references, including [10, 64, 14, 45, 47]. The PBE formulation employed in this paper is the continuous PBE in terms of particle volume, v, a description suitable for problems involving coagulation because the volume is conserved in a coagulation event and the kernel assumes a simpler form. We define the number density, $n(v,t)$, as the number of particles per unit of particle volume (and possibly per unit volume of physical space, if considered as a concentration in a spatially dependent PBE) at a time instance t. The PBE formulation for a problem involving nucleation, surface processes (such as growth and oxidation) and coagulation is:

$$\frac{\partial n}{\partial t} + \frac{\partial (Gn)}{\partial v} = B\delta(v - v_0) + \frac{1}{2}\int_0^v \beta(v-w,w)n(v-w)n(w)dw - \int_0^\infty \beta(v,w)n(v)n(w)dw \quad (1)$$

where B is the nucleation rate, G is the volumetric rate of change due to surface processes and $\beta(v,w)$ is the coagulation kernel, i.e. the function giving the rate of coagulation between particles of volumes v and w, and the dependence of n on v and t is omitted where appropriate. Coagulation is expressed via the last two terms, which represent a source and a sink, and take the form of integrals due to the need for accounting for all possible particle pairs. Together with initial conditions for the number density, the PBE constitutes an initial value problem.

The solution of the PBE poses severe challenges, arising from its integro-differential and non-linear nature. Analytical and similarity solutions can be obtained only for a few special cases, but are are useful for benchmarking numerical methods; reviews of them can be found in [10, 64, 14, 45]. Monte Carlo methods proceed by constructing an ensemble of particles and subjecting them to random events for each process in the PBE at every time step, consistent with the rate of that process (see e.g. [5]). They are very expensive computationally, because large numbers of particles are needed to obtain convergence, and hence have been used employed for kinetic investigations in ideal or partially-stirred reactors and 1-D laminar flames. The two main classes of methods that are suitable for realistic spatially dependent problems involving laminar or turbulent flow are moment and discretisation methods.

Moment methods comprise a large family of approaches that predict the moments of the distribution rather than the distribution itself. The advantage of moment methods is the reduction in the number of variables. On the other hand, there are cases where the prediction of the distribution is of interest, such as soot, where the smaller particles are more harmful for human health. Furthermore, the moment formulation is unclosed. To address the closure problem, several approaches have been proposed. One approach is based on a series expansion of the number density, first proposed in [25, 24], but has found very limited application. A second approach is to presume the shape of the distribution. This approach is used extensively in aerosols (see e.g. [65, 63]) but not often in soot, where the combination of surface processes, coagulation and aggregation as well as the effect of spatial variation of precursors gives rise to considerable variability and often bimodal features to the distribution, and thus the assumption of a presumed shape is not adequate. A third class of methods is based on obtaining the fractional moments by interpolation, first suggested in [13] and used extensively in soot - later described as Method of Moments with Interpolative Closure (MOMIC) and its variants. Finally, a fourth family of moment methods is based on approximating the moment integrals with numerical quadrature whose parameters are allowed to evolve in time, first suggested in the form of the Quadrature Method of Moments (QMOM) [34] and later as Direct Quadrature Method of Moments (DQMOM) [33] and its variants. Some methods employ a combination of these concepts, such

as the Hybrid Method of Moments (HMOM) [36] that combines MOMIC and DQMOM concepts and is used in soot modelling. Another issue with moment methods is the realisability of the moments [59], which cannot be ensured in some of the closure schemes or in the spatial transport of the moments [66, 38].

Discretisation methods aim to predict the distribution by discretising the domain of the independent variable, and do not suffer from closure issues. Several challenges, however, are encountered in developing an efficient and accurate discretisation method for the PBE. First of all, the domain spans several orders of magnitude, with different processes occurring at different scales: nucleation, for example, is a localised source appearing at the one end of the domain, while coagulation spreads the distribution towards larger sizes. Secondly, it is not straightforward to obtain a discretisation of the coagulation terms that conserves the first moment of the distribution in an arbitrary non-uniform grid. The first moment is proportional to the total particle mass, hence an error in its conservation implies an error in the mass balance. Several methods aim to accomplish conservation at the expense of accuracy in the prediction of the distribution. Finally, the growth term is a first-order derivative and can give rise to sharp fronts. Work so far has resulted in a number of solutions to these problems, but it is difficult to obtain a method that attains a balance between these objectives, a problem that stems from the fact that processes of a very different nature and mathematical behaviour (nucleation, growth and coagulation) must be accommodated.

The objective of the present work is to propose a new finite volume discretisation method for the PBE that accomplishes: a) accurate prediction of the distribution with a small number of sections, b) conservation of the first moment (or any other single moment) in a coagulation process, c) applicability to an arbitrary non-uniform grid, and d) speed and robustness that make it suitable for combining with a CFD code. Extensive testing is performed to establish the first three points, while the last point is demonstrated by means of a computation of soot formation in a laminar co-flow diffusion flame that has been investigated experimentally by Santoro et al. [52, 53].

The paper is organised as follows. An overview of existing discretisation methods for the PBE is presented first, in order to put the new method in context. Subsequently, the equations for the proposed approach approach are derived, initially for the coagulation PBE and then for nucleation and growth. The method is then tested against analytical solutions or direct numerical solutions of the discrete PBE for coagulation and coagulation-growth problems. Finally, the application to the laminar flame is presented, which involves coupling with fluid dynamics, chemical kinetics, transport phenomena and radiation.

2 Overview of discretisation methods for the PBE

A large number of approaches have been proposed for the discretisation of the PBE. In this paper we will focus on the numerical treatment of coagulation, although the method developed is for combined nucleation, growth and coagulation problems and the discretisation of nucleation and growth will also be briefly discussed. While the derivation of the various methods is based on a range of concepts, the methods can be classified into two general categories:

- Pointwise approximation methods. These methods proceed by postulating a discrete PBE where the number density is concentrated at specific points. This amounts to approximating the number density as a sum of delta functions [45]. The coefficients of this discrete PBE are then derived so as to ensure conservation of one or more moments of the distribution. Therefore these methods aim primarily at conservation of the moments, rather than accuracy in the prediction of the distribution. Unlike moment methods, however, they do not suffer from the closure problem. They can be viewed as bridging the gap between moment and discretisation methods.

- Finite element/volume methods. These methods take the PBE as the starting point, divide the domain of the independent variable into a number of intervals and approximate the number density over each

interval via a function (often a constant one). A weighted integral of the equation is then formed, and the residual over each element is minimised according to a certain rule. The finite element method provides the most general mathematical framework for deriving such methods, and the finite volume method can be obtained as a special case. Several methods that belong to this category have not, however, been derived via a finite element procedure. These methods aim at an accurate computation of the number density, but moment conservation is in general not guaranteed, unless the method is derived in a special way to ensure conservation of a particular moment.

In pointwise approximation methods the distribution is approximated as a set of delta functions, and therefore there is no need to carry out integrations of the kernel and number densities; rather, the coagulation integral terms are approximated as products of the number densities at the representative particle sizes. For example, the approximation of the source term integral for a section centred on v_i and of length δv_i can be written as:

$$\int_{v_i-\frac{\delta v_i}{2}}^{v_i+\frac{\delta v_i}{2}} \int_0^{v} \beta(v-w,w)n(v-w)n(w)dwdv \approx \sum_{\substack{j \\ v_k+v_j=v_i}} \beta_{k,j}n_k n_j \tag{2}$$

where the factors $\beta_{k,j}$ include the kernel and any other correction factors required by the approximation scheme. An inherent problem in this approach is that the sum of volumes $v_k + v_j$ will almost never be equal to the representative volume of any other interval unless a uniform grid is employed, so the resultant particle must be allocated to one of the two adjacent points and thus gain or lose volume. To counter this effect, correction factors (incorporated in $\beta_{k,j}$) are introduced so as to conserve one or two moments of the distribution. Methods in this category thus place priority on moment conservation rather than on accuracy in the prediction of the distribution.

A number of these methods are based on a grid constructed via a geometric progression, in which several simplifications are possible, particularly for coagulation-only problems. In a grid where $v_i = 2v_{i-1}$, for example, only particles from the previous point can contribute to the coagulation source term, a fact that greatly reduces the number of computations to be carried out. The geometric grid was first proposed by Bleck [7] and further developed by Marchal et al. [32] and Hounslow et al. [23]. The last of these methods conserves both number density and particle volume, but is still limited to a particular geometric grid. The most general and flexible method in this class is that of Kumar and Ramkrishna [28], [29], which solves algebraic equations to compute correction factors that conserve any two moments of the distribution and is not tied to a particular choice of grid.

The source of error in the distribution in pointwise approximation methods is demonstrated graphically in Fig. 1, referring to the Kumar and Ramkrishna method [28]. The particles are considered to be concentrated at the discrete points v_j^c, v_k^c, v_{i-1}^c, v_i^c, v_{i+1}^c (which are called *pivots* in the Kumar and Ramkrishna method). As the sum $v_j^c + v_k^c$ does not correspond to any pivot, the particles are allocated to two adjacent pivots, in this case v_i^c and v_{i+1}^c. However, the coagulating particles actually spread over the entire intervals (v_{j-1}, v_j) and (v_{k-1}, v_k) and the correct distribution of the resulting particles could be spreading further than the intervals containing v_i^c and v_{i+1}^c. For example, in this case the particle with volume $v_{j-1} + v_{k-1}$ is located in the interval (v_{i-2}, v_{i-1}).

Recently, a family of methods has been developed that share features of both moment and discretisation methods and can also be related to the methods discussed above. The Two-Size Moment (TSM) method was developed in the context of sprays [30] and particles [38], while the Multi-Moment Sectional Method (MMSM) [67] was developed in the context of soot. In these methods, the particle size domain is divided into sections and two or more moments are computed in each section, while the distribution is reconstructed from the moments. Unlike moment methods, where only a few moments are computed, methods in this class require several sections and two or more moments per section, although they offer flexibility with respect to the number of both sections and moments.

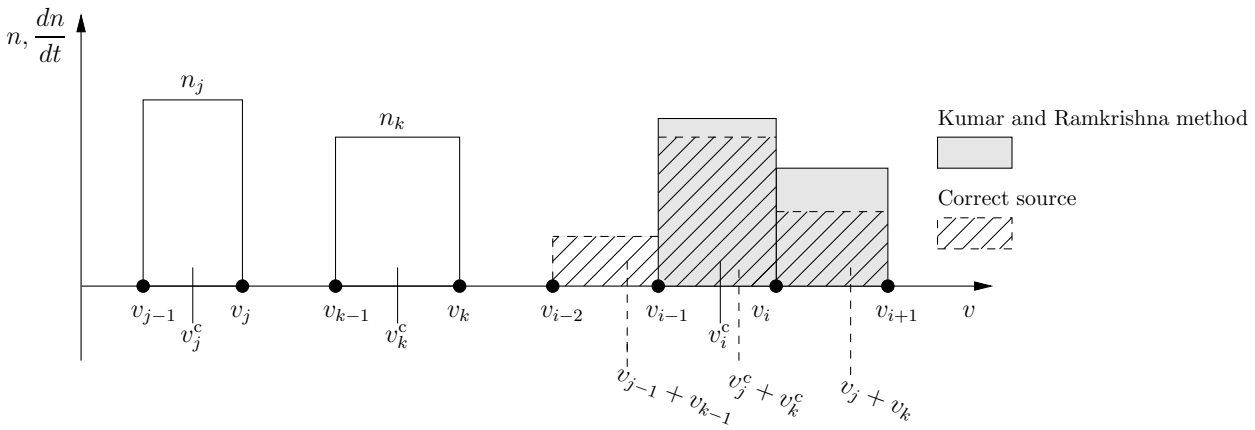

Figure 1: Error of coagulation source in Kumar and Ramkrishna method

A related approach originates in the work of Pope and Howard [40] and is also related to the 'method of classes' developed by Marchal et al. [32] in crystallisation. In this method, the particle size distribution is also discretised into sections, which are then treated as chemical species and added to the reaction mechanism, while the growth and coagulation processes are represented as chemical reactions between particles in a section and species. The method was further developed and applied to laminar premixed flames by Richter et al. [46]. One advantage of this approach is that it can be implemented in packages such as CHEMKIN in the same way as a chemical mechanism. However, there is no flexibility for changing the grid once the PBE has been implemented as a mechanism. Furthermore, treating the sections as species means that the particle size distribution must be solved together with the chemical kinetics mechanism, which is often very stiff. By contrast, the solution of the PBE as a separate equation allows the PBE discretisation to be carried out in a separate step via operator splitting.

In the second class of approaches, the distribution is first being approximated by trial functions that can be polynomials or constant functions. Gelbard and Seinfeld employed cubic splines in their earlier work [17], but abandoned that approach in favour of constant functions in their subsequent work on the coagulation equation [19] and on multicomponent coagulation and growth [18]. While initially developed for aerosols, the method described in [19] was later applied to the modelling of soot formation in laminar premixed and non-premixed flames [9, 22]. Other finite element studies used collocation and Galerkin methods [39, 51] or collocation with linear trial functions [48], but have not been applied to soot. Netzell et al. [37] developed a method that employed a linear variation for the distribution within each section, although the derivation was not based on a finite element framework. This approach was used in a number of soot modelling studies, including [49] for laminar counterflow diffusion flames, [4] for laminar premixed flames, [50] for turbulent non-premixed flames and [3] for RANS simulation of Diesel engines. Finally. the finite volume method was employed by reformulating the PBE into a hyperbolic PDE [12, 42], although this approach has not been applied to soot.

The method developed in this work is a finite volume method that can be applied to a PBE combining coagulation, nucleation and growth. The main innovation of the method lies in the treatment of the coagulation integral terms, for which a scheme is proposed that a) conserves the first moment (or any other chosen one), and b) is accurate and robust even when a small number of nodes is employed. The proposed method is combined with an accurate scheme for the discretisation of the growth term, and the overall formulation is coupled with fluid dynamics for the prediction of problems involving particle formation in flow fields, such as soot formation in flames.

3 Description of the method

3.1 An analysis of the finite volume method applied to coagulation

In the following, we will employ the PBE for a coagulation process as the starting point for the discussion of coagulation schemes, with the $(0, \infty)$ domain truncated to $(v_0, v_{\max})$, where v_0 is the minimum particle size in the coagulation process. Furthermore, it is more computationally efficient to carry out the numerical approximation of the source integral up to $\frac{v}{2}$ rather than double counting all pairs and dividing by half. The equation incorporating these changes is:

$$\frac{\partial n}{\partial t} = \int_{v_0}^{\frac{v}{2}} \beta(v-w,w)n(v-w)n(w)dw - \int_{v_0}^{v_{max}} \beta(v,w)n(v)n(w)dw \tag{3}$$

with the initial condition $n(v,t) = n_0(v)$ at $t = 0$.

To proceed with the discretisation, we define a grid in the volume space $(v_0, ..., v_n)$ and denote the intervals as $\Delta v_i = v_i - v_{i-1}$. Since the particle volume typically covers a very wide range in most problems - e.g. for aerosols it can range from 1 nm - 1 μm in diameter, hence nine orders of magnitude in volume - a non-uniform grid must be employed, typically expanding towards increasing volume. While many of the methods developed are tied to a geometric grid, the present method is developed for an arbitrary grid and could also be combined with an adaptive grid, such as the method developed in [56] and applied to aerosols and soot in [57, 58, 55].

To employ the finite volume method, the number density over each interval must first be approximated with a simple function. The zeroth order approximation (constant number density) is employed here, because it will facilitate the analysis and control of the conservation properties of the scheme. It must be noted that this approximation is akin to a histogram, which is the form in which distributions are obtained experimentally. The number density is thus assigned a constant value n_i over each interval Δv_i. Subsequently, Eq. 3 is integrated over the interval Δv_i to obtain:

$$\frac{dn_i}{dt} = \frac{1}{\Delta v_i}\int_{v_{i-1}}^{v_i}\left(\int_{v_0}^{\frac{v}{2}} \beta(v-w,w)n(v-w)n(w)dw\right)dv - \frac{1}{\Delta v_i}\int_{v_{i-1}}^{v_i}\left(\int_{v_0}^{v_{\max}} \beta(v,w)n(w)dw\right)n(v)dv \tag{4}$$

The PBE has now been converted into a system of integro-differential equations describing the temporal evolution of the discretised number density. If the integral terms can be approximated, it will be possible to integrate the resulting equations with respect to time and obtain $n_i(t)$.

At this point, we are faced with the approximation of two integrations: one over the finite volume interval Δv_i and one over the domain that yields the pair combinations. One approach would be to employ a quadrature rule for the first integration. However, any such rule would result in an error in the distribution. Consider, for instance, the trapezoid rule. For the source term, this rule would give:

$$\begin{aligned}\left.\frac{dn_i}{dt}\right|_{\text{source}} =& \frac{1}{\Delta v_i}\int_{v_{i-1}}^{v_i}\left(\int_{v_0}^{\frac{v}{2}} \beta(v-w,w)n(v-w)n(w)dw\right)dv \\ \approx& \frac{1}{2}\left(\int_{v_0}^{\frac{v_{i-1}}{2}} \beta(v_{i-1}-w,w)n(v_{i-1}-w)n(w)dw + \int_{v_0}^{\frac{v_i}{2}} \beta(v_i-w,w)n(v_i-w)n(w)dw\right) \\ =& \frac{1}{2}\left(\left.\frac{dn(v_{i-1})}{dt}\right|_{\text{source}} + \left.\frac{dn(v_i)}{dt}\right|_{\text{source}}\right)\end{aligned} \tag{5}$$

The error is illustrated via an example in Fig. 2, where we consider the coagulation process between intervals $(v_{j-1},\ v_{j+1})$ and $(v_{k-1},\ v_{k+1})$ respectively. A non-uniform grid is employed, where the smallest possible

interval is (v_j,v_{j+1}) or its equal (v_{k-1},v_k), and this interval is taken as a unit for subdividing all other intervals into sub-intervals. The plot shows both the distribution and the coagulation source (on the positive axis) and sink (on the negative axis) terms. The shaded areas with the same pattern indicate corresponding sources and sinks. The error of the two-point quadrature scheme is evident. While a multi-point quadrature scheme would reduce the error, it would still not be conservative.

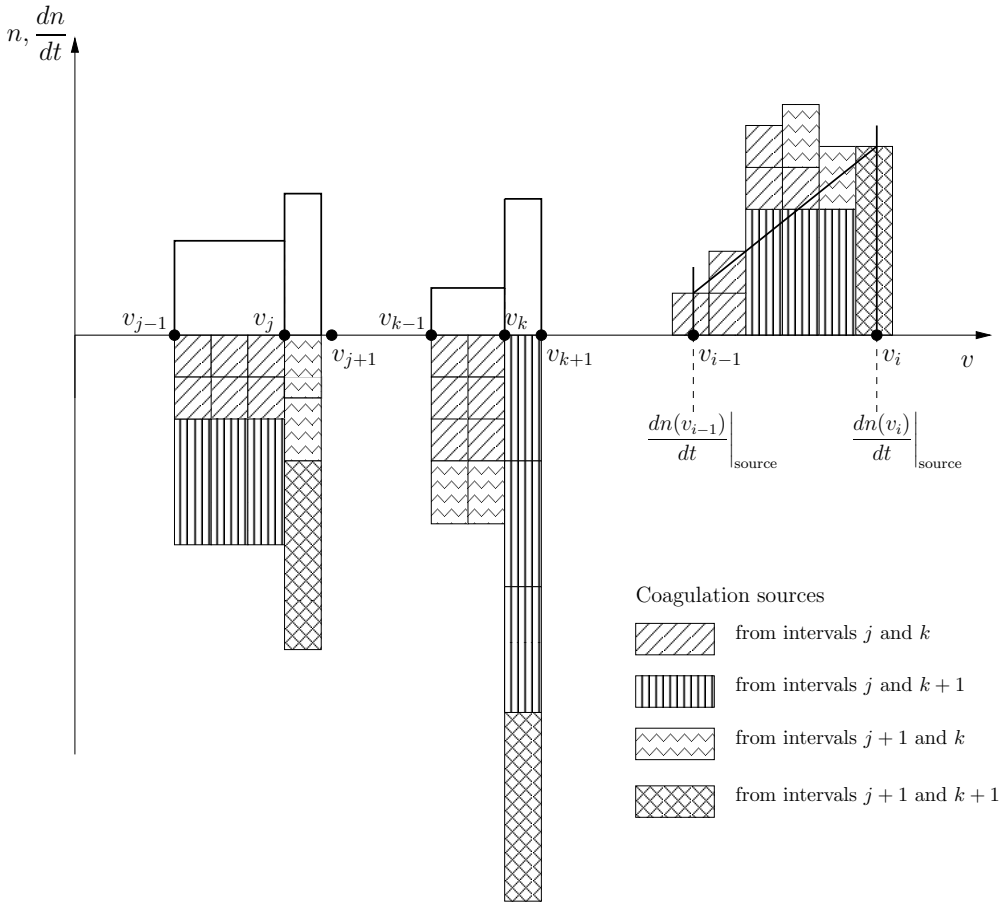

Figure 2: Error in the evaluation of the coagulation term with two-point quadrature

3.2 A conservative finite volume approach for coagulation

In finite volume schemes for fluid dynamics, conservation is ensured because the fluxes from one cell are entering into a neighbouring cell. While conservation alone does not guarantee accuracy, it is a highly desired property for a numerical method intended for solution of the fluid dynamics equations and has contributed to the widespread use of finite volume methods in that field. In the PBE, conservation of the first moment of a distribution with respect to particle volume is important because a) it is an invariant in a coagulation process and b) it represents conservation of mass. However, the application of the finite volume method alone does not guarantee conservation in a PBE solution scheme, as has been shown in Fig. 2. Unlike fluid dynamics, in coagulation the fluxes into an interval may arise from everywhere in the domain, and not just from the adjacent intervals.

In order to derive a conservative numerical scheme, it must be ensured that the sources and sinks balance each other. In the case of the PBE, application of this principle means that the particles removed from one interval due to coagulation should be added to another interval, i.e. the shaded areas in Fig. 2 should corre-

spond to each other. In the following, we will be guided by this principle in order to derive a conservative finite volume discretisation for the coagulation terms in the PBE. To accomplish this, only the sink terms will be calculated and subsequently mapped to the source terms.

At this point, it is worth comparing with pointwise approximation methods such as [28]. In these methods, the distribution is modified to ensure the conservation of one or more moments due to the fact that the particles can only be allocated at grid points (Fig. 1). In the proposed method, the primary aim is to predict correctly the distribution, which is why we consider the number density as spreading over whole intervals rather than concentrated at single points. The conservation of one moment is ensured by the balancing of source and sink terms, while other moments can be expected to be accurate as a result of the accurate prediction of the distribution.

We will now proceed to derive a finite volume scheme that is conservative with respect to the first moment. We first multiply Eq. 3 by v and integrate over an interval, leading to the following finite volume equation for the balance of the particle volume in interval i. It must be noted that one may multiply by v^m instead and conserve an arbitrary moment of order m; indeed, results for conservation of both the zeroth and first moment will be shown in Sec. 4. The equation for the first moment is:

$$\frac{d}{dt}\int_{v_{i-1}}^{v_i} vn(v)dv = \int_{v_{i-1}}^{v_i} v\frac{dn(v)}{dt}dv$$
$$= \frac{1}{\Delta v_i}\int_{v_{i-1}}^{v_i}\left(\int_{v_0}^{\frac{v}{2}}\beta(v-w,w)n(v-w)n(w)dw\right)vdv - \frac{1}{\Delta v_i}\int_{v_{i-1}}^{v_i}\left(\int_{v_0}^{v_{\max}}\beta(v,w)n(w)dw\right)n(v)vdv \tag{6}$$

3.3 The main steps of the method

The main steps of the method can now be summarised as follows.

- **Determination of complementary points.** For each interval i denoting the range $[v_{i-1}, v_i]$, and for each interval $j(i)$ denoting the range $[w_{j-1}(i), w_j(i)]$ where $w_{j-1} < \dfrac{v(i)}{2}$ (note that both v and w will be used to represent volume), we locate four points, which will hence be called the *complementary points*, and which correspond to the volumes of particles that would coagulate with particles at the boundaries of j to form particles at the boundaries of i (Fig. 3), as follows:

$$\mathrm{U}_{i-1,j} = v_{i-1} - w_j \tag{7a}$$
$$\mathrm{U}_{i-1,j-1} = v_{i-1} - w_{j-1} \tag{7b}$$
$$\mathrm{U}_{i,j} = v_i - w_j \tag{7c}$$
$$\mathrm{U}_{i,j-1} = v_i - w_{j-1} \tag{7d}$$

  The auxiliary grid of complementary points is evaluated at the beginning of the simulation and stored, so no CPU time is spent on this step during the simulation.

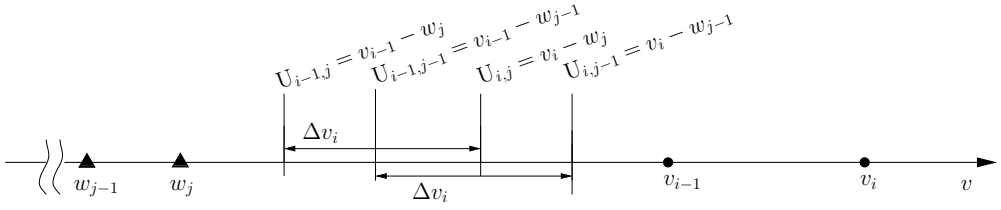

Figure 3: The auxiliary grid of complementary points

- **Evaluation of source and sink terms.** At each time step, the double integrals representing the sources and sinks due to coagulation of particles in $[w_{j-1}, w_j]$ with particles in the range spanned by the complementary points and resulting in particles in $[v_{i-1}, v_i]$ are evaluated geometrically, according to a procedure that will be described in detail in Secs. 3.4.1, 3.4.2. Only the sink terms are calculated, and the source terms of the resulting particles are incremented accordingly. This way, the source and sink terms balance and conservation of the first moment is ensured.

- **Temporal integration.** Once all source and sink terms have been evaluated, a set of ODEs for the number density in each interval is assembled and integrated over a time interval δt to calculate the discretised distribution at $t + \delta t$.

3.4 Derivation of the discretised equations for coagulation

Before we begin with the derivation of the discretised equations, a partitioning of the intervals is formed, separating the intervals up to $\frac{v}{2}$ is formed as follows:

$$\begin{aligned} G_1(i) &= \left\{ [v_1, v_2], \cdots, \left[v_{k-1}(i), \frac{v_{i-1}}{2} \right] \right\} \\ G_2(i) &= \left\{ \left[\frac{v_{i-1}}{2}, v_k(i) \right], ..., \left[v_l(i), \frac{v_i}{2} \right] \right\} \end{aligned} \tag{8}$$

where is the maximum nodal volume smaller than $\frac{v_{i-1}}{2}$, v_k is the minimum one greater than $\frac{v_{i-1}}{2}$ and v_l is the maximum one smaller than $\frac{v_i}{2}$. The set $G_1(i)$ thus contains all the intervals within $\left[v_0, \frac{v_{i-1}}{2} \right]$, while the set $G_2(i)$ contains all the intervals within $\left[\frac{v_{i-1}}{2}, \frac{v_i}{2} \right]$ (Fig. 4). Note that the last interval of $G_1(i)$ and the first and last intervals of $G_2(i)$ are actually fractions of intervals, as they are bounded by the values $\frac{v_{i-1}}{2}$, $\frac{v_i}{2}$ which are not, in general, nodal values. The reason for this classification is because, as we will see, a different treatment is required for the intervals in $G_2(i)$. This feature results from formulating the source term as an integral from 0 to $\frac{v}{2}$; while it increases the complexity of the discretisation scheme, it reduces the computational time by half.

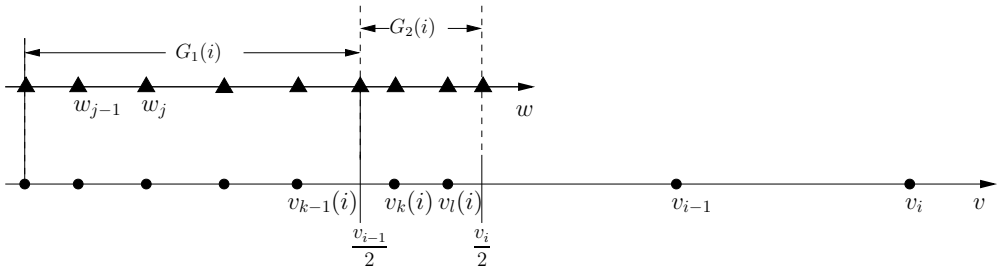

Figure 4: The two groups of intervals $G_1(i)$ and $G_2(i)$

We will now proceed to show the detailed derivation of the discretised equations. For brevity, we define:

$$C(v, w) = \beta(v, w) n(v) n(w) \tag{9}$$

The source term will now be split into two parts, one resulting from coagulation in the intervals in $G_1(i)$

and one from those in $G_2(i)$:

$$\left(\frac{d}{dt}\int_{v_{i-1}}^{v_i} vn(v)dv\right)\Big|_{\text{source}} = \int_{v_{i-1}}^{v_i}\left(\int_{v_0}^{\frac{v_{i-1}}{2}} C(v-w,w)dw\right)vdv + \int_{v_{i-1}}^{v_i}\left(\int_{\frac{v_{i-1}}{2}}^{\frac{v}{2}} C(v-w,w)dw\right)vdv \tag{10}$$

The inner integrals in Eq. 10 can be written as summations over the intervals spanning the ranges $G_1(i)$ and $G_2(i)$:

$$\int_{v_{i-1}}^{v_i}\left(\sum_{G_1(i)}\int_{w_{j-1}}^{w_j} C(v-w,w)dw\right)vdv = \sum_{G_1(i)}\int_{v_{i-1}}^{v_i}\left(\int_{w_{j-1}}^{w_j} C(v-w,w)dw\right)vdv = \sum_{j\in G_1(i)} I_{b1}(i,j) \tag{11a}$$

$$\begin{aligned}\int_{v_{i-1}}^{v_i}\left(\int_{\frac{v_{i-1}}{2}}^{v} C(v-w,w)dw\right)vdv &= \int_{\frac{v_{i-1}}{2}}^{\frac{v_i}{2}}\left(\int_{2w}^{v_i} vC(v-w,w)dv\right)dw \\ &= \sum_{j\in G_2(i)}\int_{w_{j-1}}^{w_j}\left(\int_{2w}^{v_i} vC(v-w,w)dv\right)dw = \sum_{j\in G_2(i)} I_{b2}(i,j)\end{aligned} \tag{11b}$$

Therefore the integrals $I_{b1}(i,j)$ and $I_{b2}(i,j)$ denote the source, or birth, of particles in interval i belonging to $G_1(i)$ or $G_2(i)$ respectively, arising from coagulation of particles in interval $j(i)$. The calculation of these integrals will be treated in the following two subsections.

3.4.1 Evaluation of source and sink terms for all intervals in $G_1(i)$

In the following, we consider the case $\Delta v_i > \Delta w_j$, so that $\mathrm{U}_{i-1,j-1} < \mathrm{U}_{i,j}$, which corresponds to an expanding grid that would normally be employed in a coagulation problem (although the method can be applied to an arbitrary grid). By introducing a change of variable $u = v - w$, the double integral $I_{\mathrm{b1}}(i,j)$ becomes:

$$\begin{aligned}I_{\mathrm{b1}}(i,j) &= \int_{v_{i-1}-w}^{v_i-w}\left(\int_{w_{j-1}}^{w_j}(u+w)C(u,w)dw\right)du \\ &= \int_{w_{j-1}}^{w_j}\left(\int_{v_{i-1}-w}^{\mathrm{U}_{i-1,j-1}}(u+w)C(u,w)du\right)dw + \int_{w_{j-1}}^{w_j}\left(\int_{\mathrm{U}_{i-1,j-1}}^{\mathrm{U}_{i,j}}(u+w)C(u,w)du\right)dw \\ &\quad + \int_{w_{j-1}}^{w_j}\left(\int_{\mathrm{U}_{i,j}}^{v_i-w}(u+w)C(u,w)du\right)dw \\ &= \Delta M_{\mathrm{b}}^{\mathrm{left}}(i,j) + \Delta M_{\mathrm{b}}^{\mathrm{middle}}(i,j) + \Delta M_{\mathrm{b}}^{\mathrm{right}}(i,j)\end{aligned} \tag{12}$$

where the notation ('left', 'middle' and 'right') corresponds to the shapes in Fig. 5.

The source of particles in $[i-1,i]$ results in sink or particles in $[j-1,j]$ and in the whole range of intervals spanned by the complementary points. Therefore there are two contributions to the sink term, which will be denoted I_{dj1} for the contribution to the sink of particles in $[j-1,j]$ and I_{dk1} for that in the complementary intervals. These are calculated as follows:

$$I_{\mathrm{b1}}(i,j) = \int_{v_{i-1}-w}^{v_i-w}\left(\int_{w_{j-1}}^{w_j} wC(u,w)du\right)dw + \int_{v_{i-1}-w}^{v_i-w}\left(dw\int_{w_{j-1}}^{w_j} uC(u,w)du\right)dw$$

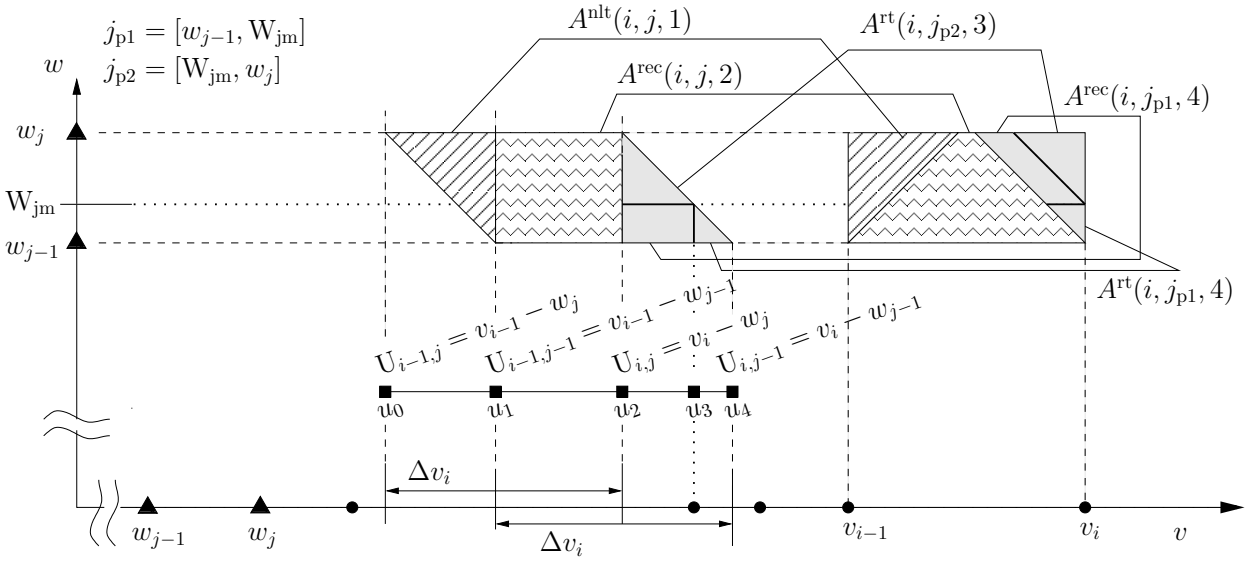

Figure 5: Locations of complementary volumes and number changes for the coagulation of intervals in $G_1(i)$.

$$
\begin{aligned}
&= I_{\mathrm{dj1}}(i,j) + I_{\mathrm{dk1}}(i,j) \qquad (13)\\
&= \sum_{\mathrm{loc}} \Delta M_{\mathrm{dj}}^{\mathrm{loc}}(i,j) + \sum_{\mathrm{loc}} \Delta M_{\mathrm{dk}}^{\mathrm{loc}}(i,j) \qquad \mathrm{loc} = (\mathrm{left}, \mathrm{middle}, \mathrm{right})
\end{aligned}
$$

The method now proceeds via a geometric interpretation of the coagulation terms, as shown in Fig. 5. The block spanned by the complementary points can be divided into three components: the left part $[\mathrm{U}_{i-1,j}, \mathrm{U}_{i-1,j-1}]$, the middle part $[\mathrm{U}_{i-1,j-1}, \mathrm{U}_{i,j}]$ and the right part $[\mathrm{U}_{i,j}, \mathrm{U}_{i,j-1}]$. In the middle part, each particle can select its coagulation partner from all particles inside the interval j $[w_{j-1}, w_j]$. This is not the case with the other parts, however: e.g. for a boundary point, in order for the resulting particle to fall within the target interval i $[v_{i-1}, v_i]$, the largest particle of size $\mathrm{U}_{i,j-1}$ can only coagulate with the smallest particle w_{j-1} within interval j. The coagulation events thus correspond to three different shaded areas: the 'normal' left triangle 'nlt' (to distinguish from the overlapping triangles, to be defined later), the rectangle 'rec' and the right triangle 'rt'. These terms constitute the integrals $I_{\mathrm{b1}}(i,j)$ and $I_{\mathrm{dj1}}(i,j)$.

To evaluate the integral $I_{\mathrm{dk1}}(i,j)$, we employ the auxiliary grid $[u_{k-1}, u_k]$, $k = 1, 2, \cdots, k_{\max}(i,j)$ within the complementary interval. Fig. 5 shows a case with $k_{\max}(i,j) = 4$. If the complementary interval spans over more intervals, it will be broken into more shapes that will be evaluated in the same way.

We now formulate the contribution of the coagulation source and sink within the geometric shapes, taking advantage of the fact that the number densities n_j^u and n_k^w are constant for each coagulation pair, $[w_{j-1}, w_j]$ and $[u_{k-1}, u_k]$. For example, let us show in detail how the source and sink terms are evaluated for the case shown in Fig. 5. We first evaluate $I_{\mathrm{dj1}}(i,j)$. The left and middle contributions are calculated as:

$$\Delta M_{\mathrm{dj}}^{\mathrm{left}}(i,j) = \int_{w_{j-1}}^{w_j} \left(\int_{v_{i-1}-w}^{\mathrm{U}_{i-1,j-1}} C(u,w)du \right) wdw = n_j^w n_1^u \int_{w_{j-1}}^{w_j} \left(\int_{v_{i-1}-w}^{u_1} \beta(u,w)du \right) wdw \quad (14a)$$

$$\Delta M_{\mathrm{dj}}^{\mathrm{middle}}(i,j) = \int_{w_{j-1}}^{w_j} \left(\int_{\mathrm{U}_{i-1,j-1}}^{\mathrm{U}_{i,j}} C(u,w)du \right) wdw = n_j^w n_1^u \int_{w_{j-1}}^{w_j} \left(\int_{u_1}^{u_2} \beta(u,w)du \right) wdw \quad (14b)$$

At this point, it only remains to evaluate the integrations of the kernel. For maximal accuracy these should be evaluated by multi-point numerical quadrature, but a simpler way is to evaluate them at the centre of weight

in each geometrical shape, and our tests show that the accuracy obtained is already very good (Sec. 4). This choice is also anticipating the application of the method to spatially-dependent problems such as soot formation: while implementing a multi-point quadrature scheme is straightforward and could be tabulated when the method is applied to the homogeneous PBE, it would incur extra computational cost when coupled with flow in a flame because the temperature dependence of the kernels would require them to be evaluated at every time step. The expressions are as follows:

$$\begin{aligned}\Delta M_{\mathrm{dj}}^{\mathrm{left}}(i,j) &= n_j^w n_1^u \beta^{\mathrm{nlt}} \int_{w_{j-1}}^{w_j} \left(\int_{v_{i-1}-w}^{u_1} du \right) w dw = n_j^w n_1^u \beta^{\mathrm{nlt}}(i,j,1) \cdot \omega_{\mathrm{dj}}^{\mathrm{nlt}}(i,j,1) \cdot A^{\mathrm{nlt}}(i,j,1) \\ &= \Delta M_{\mathrm{dj}}^{\mathrm{nlt}}(i,j,1) \end{aligned} \tag{15a}$$

$$\begin{aligned}\Delta M_{\mathrm{dj}}^{\mathrm{middle}}(i,j) &= n_j^w n_2^u \beta^{\mathrm{rec}} \int_{w_{j-1}}^{w_j} \left(\int_{u_1}^{u_2} du \right) w dw = n_j^w n_2^u \beta^{\mathrm{rec}}(i,j,2) \cdot \omega_{\mathrm{dj}}^{\mathrm{rec}}(i,j,1) \cdot A^{\mathrm{rec}}(i,j,2) \\ &= \Delta M_{\mathrm{dj}}^{\mathrm{rec}}(i,j,2) \end{aligned} \tag{15b}$$

The parameters in Eq. 15, namely the evaluated kernel β^{shape}, the weight of centres $\omega_{\mathrm{dj}}^{\mathrm{shape}}$, the integral area A^{shape} and the volume change in corresponding integral area $M_{\mathrm{dj}}^{\mathrm{shape}}$, where $\mathrm{shape} = \mathrm{nlt(olt)}, \mathrm{rec}, \mathrm{rt}$, are all functions of interval i, interval $k(i,j)$ and subinterval $j_{\mathrm{p}}(i,j,k)$. These terms are pre-computed and tabulated, and their expressions for all discretised terms are given in Table 1. In the same way, we can also obtain the volume change due to the coagulation process between the interval j and the right part of its complementary block. Note that since, in this case, the right part covers different intervals k, a volume point $\mathrm{W_{jm}} = v_i - u_3$ can be found in Fig. 5 and this double integral is composed of several shapes:

$$\begin{aligned}\Delta M_{\mathrm{dj}}^{\mathrm{right}}(i,j) &= n_j^w n_3^u \beta^{\mathrm{rt}}(i,j_{\mathrm{p2}},3) \cdot \omega_{\mathrm{dj}}^{\mathrm{rt}}(i,j_{\mathrm{p2}},3) \cdot A^{\mathrm{rt}}(i,j_{\mathrm{p2}},3) \\ &\quad + n_j^w n_3^u \beta^{\mathrm{rec}}(i,j_{\mathrm{p1}},3) \cdot \omega_{\mathrm{dj}}^{\mathrm{rec}}(i,j_{\mathrm{p1}},3) \cdot A^{\mathrm{rec}}(i,j_{\mathrm{p1}},3) \\ &\quad + n_j^w n_4^u \beta^{\mathrm{rt}}(i,j_{\mathrm{p1}},4) \cdot \omega_{\mathrm{dj}}^{\mathrm{rt}}(i,j_{\mathrm{p1}},4) \cdot A^{\mathrm{rt}}(i,j_{\mathrm{p1}},4) \\ &= \Delta M_{\mathrm{dj}}^{\mathrm{rt}}(i,j_{\mathrm{p2}},3) + \Delta M_{\mathrm{dj}}^{\mathrm{rec}}(i,j_{\mathrm{p1}},3) + \Delta M_{\mathrm{dj}}^{\mathrm{rt}}(i,j_{\mathrm{p1}},4) \end{aligned} \tag{15c}$$

where j_{p1} and j_{p2} are subintervals of interval j, representing $[w_{j-1}, \mathrm{W_{jm}}]$ and $[\mathrm{W_{jm}}, \mathrm{w_j}]$, respectively. The integral $I_{\mathrm{dj1}}(i,j)$ is finally composed of:

$$I_{\mathrm{dj1}}(i,j) = \Delta M_{\mathrm{dj}}^{\mathrm{nlt}}(i,j,1) + \Delta M_{\mathrm{dj}}^{\mathrm{rec}}(i,j,2) + \Delta M_{\mathrm{dj}}^{\mathrm{rt}}(i,j_{\mathrm{p2}},3) + \Delta M_{\mathrm{dj}}^{\mathrm{rec}}(i,j_{\mathrm{p1}},3) + \Delta M_{\mathrm{dj}}^{\mathrm{rt}}(i,j_{\mathrm{p1}},4) \tag{16a}$$

Similarly, for $I_{\mathrm{dk1}}(i,j)$:

$$I_{\mathrm{dk1}}(i,j) = \Delta M_{\mathrm{dk}}^{\mathrm{nlt}}(i,j,1) + \Delta M_{\mathrm{dk}}^{\mathrm{rec}}(i,j,2) + \Delta M_{\mathrm{dk}}^{\mathrm{rt}}(i,j_{\mathrm{p2}},3) + \Delta M_{\mathrm{dk}}^{\mathrm{rec}}(i,j_{\mathrm{p1}},3) + \Delta M_{\mathrm{dk}}^{\mathrm{rt}}(i,j_{\mathrm{p1}},4) \tag{16b}$$

while the source term is equal to the sum of the two sink terms.

3.4.2 Evaluation of source and sink terms for all intervals in $G_2(i)$

We now consider the intervals $j = [w_{j-1}, w_j]$ inside group $G_2(i)$, where $j \in \left[\frac{v_{i-1}}{2}, \frac{v_i}{2}\right]$. The same strategy is employed to solve the double integrals $I_{b2}(i,j)$. Let $u = v - w > w$:

$$\begin{aligned} I_{\mathrm{b2}}(i,j) &= \int_{w_{j-1}}^{w_j} \left(\int_{2w}^{v_i} vC(v-w,w)dv \right) dw \\ &= \int_{w}^{v_i - w} \left(\int_{w_{j-1}}^{w_j} (w+u)C(u,w)dw \right) du \\ &= \int_{w_{j-1}}^{w_j} \left[\int_{w}^{\mathrm{U}_{i-1,j-1}} (w+u)du + \int_{\mathrm{U}_{i-1,j-1}}^{\mathrm{U}_{i,j}} (w+u)du + \int_{\mathrm{U}_{i,j}}^{v_i - w} (w+u)du \right] C(u,w)dw \\ &= \sum_{\mathrm{loc}} \Delta M_{\mathrm{b}}^{\mathrm{loc}}(i,j) \qquad (\mathrm{loc} = \mathrm{left}, \mathrm{middle}, \mathrm{right}) \\ &= \sum_{\mathrm{loc}} \Delta M_{\mathrm{dj}}^{\mathrm{loc}}(i,j) + \sum_{\mathrm{loc}} \Delta M_{\mathrm{dk}}^{\mathrm{loc}}(i,j) \end{aligned} \tag{17}$$

As Fig. 6 shows, the left wing $[\mathrm{U}_{i-1,j}, \mathrm{U}_{i-1,j-1}]$ completely belongs to interval j and the particle of size $w \in [w_{j-1}, w_j]$ can coagulate with any larger complementary particle inside $[w, w_j]$. Therefore, we name the integral shape for the left part 'overlapping left triangle' (olt) and all related parameters are displayed in Table 1.

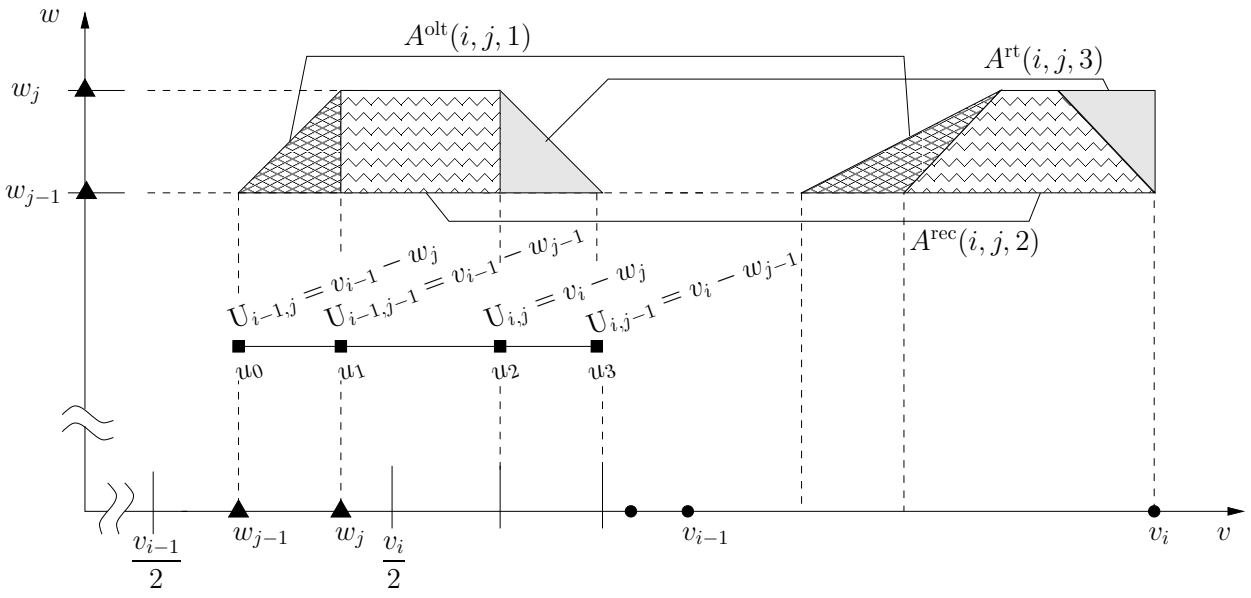

Figure 6: Locations of complementary volumes and number changes for the coagulation of intervals in $G_2(i)$

$$\Delta M_{\mathrm{dj}}^{\mathrm{left}} = \Delta M_{\mathrm{dj}}^{\mathrm{olt}}(i,j,1) = n_j^w n_1^u C^{\mathrm{olt}}(i,j,1)\omega_{\mathrm{dj}}^{\mathrm{olt}}(i,j,1)A^{\mathrm{olt}}(i,j,1) \tag{18}$$

3.5 Final assembly of terms

Once all of the source and sink terms have been evaluated, the following set of ODEs can be assembled:

$$\frac{dn_i}{dt} = \frac{1}{\Delta v_i \bar{v}_i} \frac{d}{dt} \int_{v_{i-1}}^{v_i} n(v) v dv$$

Shape		$\Delta M_m(i, j_\mathrm{p}, k)$	A	$\Delta N(i, j_\mathrm{p}, k)$	$\Delta M(i, j_\mathrm{p}, k)$	Weight centres ω	C
Right triangles ('rt')	j	$\Delta M^{\mathrm{rt}}_{m,\mathrm{dj}} = C^{\mathrm{rt}}\left[\frac{{w_{\mathrm{jr}}}^{m+2} - {w_{\mathrm{jl}}}^{m+2}}{(m+1)(m+2)} - \frac{h\cdot {w_{\mathrm{jl}}}^{m+1}}{m+1}\right]$	$A^{\mathrm{rt}} = \frac{1}{2}h^2$	$\left.\begin{matrix}\left\|\Delta N^{\mathrm{rt}}_{\mathrm{dj}}\right\| \\ \left\|\Delta N^{\mathrm{rt}}_{\mathrm{dk}}\right\| \\ \Delta N^{\mathrm{rt}}_{\mathrm{b}}\end{matrix}\right\} = A^{\mathrm{rt}}C^{\mathrm{rt}}$	$\Delta M^{\mathrm{rt}}_{\mathrm{dj}} = \omega^{\mathrm{rt}}_{\mathrm{dj}}\Delta N^{\mathrm{rt}}_{\mathrm{dj}}$	$\omega^{\mathrm{rt}}_{\mathrm{dj}} = w_{\mathrm{jl}} + \frac{1}{3}h$	
	k	$\Delta M^{\mathrm{rt}}_{m,\mathrm{dk}} = \frac{h_j\cdot C^{\mathrm{rt}}}{m+1}({u_k}^{m+1} - {u_{k-1}}^{m+1})$			$\Delta M^{\mathrm{rt}}_{\mathrm{dk}} = \omega^{\mathrm{rt}}_{\mathrm{dk}}\Delta N^{\mathrm{rt}}_{\mathrm{dk}}$	$\omega^{\mathrm{rt}}_{\mathrm{dk}} = u_k - \frac{2}{3}h$	$C^{\mathrm{rt}} = n_j^w n_k^u \beta\left(\omega^{\mathrm{rt}}_{\mathrm{dj}}, \omega^{\mathrm{rt}}_{\mathrm{dk}}\right)$
	i	$\Delta M^{\mathrm{rt}}_{m,\mathrm{b}} = C^{\mathrm{rt}}\left[\frac{(v_{\mathrm{jl}}+v_{\mathrm{kl}})^{m+2} - (v_{\mathrm{jl}}+v_{\mathrm{kr}})^{m+2}}{(m+1)(m+2)} + \frac{h\cdot(v_{\mathrm{jl}}+v_{\mathrm{kr}})^{m+1}}{m+1}\right]$		$\Delta N^{\mathrm{rt}}_{\mathrm{b}}$	$\Delta M^{\mathrm{rt}}_{\mathrm{b}} = \omega^{\mathrm{rt}}_{\mathrm{b}}\Delta N^{\mathrm{rt}}_{\mathrm{b}}$	$\omega^{\mathrm{rt}}_{\mathrm{b}} = \omega^{\mathrm{rt}}_{\mathrm{dj}} + \omega^{\mathrm{rt}}_{\mathrm{dk}}$	
Rectangles ('rec')	j	$\Delta M^{\mathrm{rec}}_{m,\mathrm{dj}} = \frac{h_k\cdot C^{\mathrm{rec}}}{m+1}({w_{\mathrm{jr}}}^{m+1} - {w_{\mathrm{jl}}}^{m+1})$	$A^{\mathrm{rec}} = h\cdot h_k$	$\left.\begin{matrix}\left\|\Delta N^{\mathrm{rec}}_{\mathrm{dj}}\right\| \\ \left\|\Delta N^{\mathrm{rec}}_{\mathrm{dk}}\right\| \\ \Delta N^{\mathrm{rec}}_{\mathrm{b}}\end{matrix}\right\} = A^{\mathrm{rec}}C^{\mathrm{rec}}$	$\Delta M^{\mathrm{rec}}_{\mathrm{dj}} = \omega^{\mathrm{rec}}_{\mathrm{dj}}\Delta N^{\mathrm{rec}}_{\mathrm{dj}}$	$\omega^{\mathrm{rec}}_{\mathrm{dj}} = w_{\mathrm{jl}} + \frac{1}{2}h$	
	k	$\Delta M^{\mathrm{rec}}_{m,\mathrm{dk}} = \frac{h\cdot C^{\mathrm{rec}}}{m+1}({u_k}^{m+1} - {u_{k-1}}^{m+1})$			$\Delta M^{\mathrm{rec}}_{\mathrm{dk}} = \omega^{\mathrm{rec}}_{\mathrm{dk}}\Delta N^{\mathrm{rec}}_{\mathrm{dk}}$	$\omega^{\mathrm{rec}}_{\mathrm{dk}} = u_k - \frac{1}{2}h_k$	$C^{\mathrm{rec}} = n_j^w n_k^u \beta(\omega^{\mathrm{rec}}_{\mathrm{dj}}, \omega^{\mathrm{rec}}_{\mathrm{dk}})$
	i	$\Delta M^{\mathrm{rec}}_{m,\mathrm{b}} = \frac{C^{\mathrm{rec}}}{(m+1)(m+2)}\Big[(w_{\mathrm{jr}}+u_k)^{m+1} - (w_{\mathrm{jr}}+u_{k-1})^{m+1} - (w_{\mathrm{jl}}+u_k)^{m+1} + (w_{\mathrm{jl}}+u_{k-1})^{m+1}\Big]$		$\Delta N^{\mathrm{rec}}_{\mathrm{b}}$	$\Delta M^{\mathrm{rec}}_{\mathrm{b}} = \omega^{\mathrm{rec}}_{\mathrm{b}}\Delta N^{\mathrm{rec}}_{\mathrm{b}}$	$\omega^{\mathrm{rec}}_{\mathrm{b}} = \omega^{\mathrm{rec}}_{\mathrm{dj}} + \omega^{\mathrm{rec}}_{\mathrm{dk}}$	
Normal left triangles ('nlt')	j	$\Delta M^{\mathrm{nlt}}_{m,\mathrm{dj}} = C^{\mathrm{nlt}}\left[\frac{{u_{\mathrm{jl}}}^{m+2} - u_{\mathrm{jl}}{u_{\mathrm{jr}}}^{m+1}}{(m+1)(m+2)} + \frac{h\cdot {u_{\mathrm{jr}}}^{m+1}}{m+2}\right]$	$A^{\mathrm{nlt}} = \frac{1}{2}h^2$	$\left.\begin{matrix}\left\|\Delta N^{\mathrm{nlt}}_{\mathrm{dj}}\right\| \\ \left\|\Delta N^{\mathrm{nlt}}_{\mathrm{dk}}\right\| \\ \Delta N^{\mathrm{nlt}}_{\mathrm{b}}\end{matrix}\right\} = A^{\mathrm{nlt}}C^{\mathrm{nlt}}$	$\Delta M^{\mathrm{nlt}}_{\mathrm{dj}} = \omega^{\mathrm{nlt}}_{\mathrm{dj}}\Delta N^{\mathrm{nlt}}_{\mathrm{dj}}$	$\omega^{\mathrm{nlt}}_{\mathrm{dj}} = w_{\mathrm{jr}} - \frac{1}{3}h$	
	k	$\Delta M^{\mathrm{nlt}}_{m,\mathrm{dk}} = C^{\mathrm{nlt}}\left[\frac{h\cdot {u_k}^{m+1}}{m+1} - \frac{{u_k}^{m+2} - {u_{k-1}}^{m+2}}{(m+1)(m+2)}\right]$			$\Delta M^{\mathrm{nlt}}_{\mathrm{dk}} = \omega^{\mathrm{nlt}}_{\mathrm{dk}}\Delta N^{\mathrm{nlt}}_{\mathrm{dk}}$	$\omega^{\mathrm{nlt}}_{\mathrm{dk}} = u_k - \frac{1}{3}h$	$C^{\mathrm{nlt}} = n_j^w n_k^u \cdot \beta(\omega^{\mathrm{nlt}}_{\mathrm{dj}}, \omega^{\mathrm{nlt}}_{\mathrm{dk}})$
	i	$\Delta M^{\mathrm{nlt}}_{m,\mathrm{b}} = C^{\mathrm{nlt}}\left[\frac{(w_{\mathrm{jr}}+u_k)^{m+2} - (w_{\mathrm{jl}}+u_k)^{m+2}}{(m+1)(m+2)} + \frac{h\cdot(w_{\mathrm{jl}}+u_k)^{m+1}}{m+2}\right]$		$\Delta N^{\mathrm{nlt}}_{\mathrm{b}}$	$\Delta M^{\mathrm{nlt}}_{\mathrm{b}} = \omega^{\mathrm{nlt}}_{\mathrm{b}}\Delta N^{\mathrm{nlt}}_{\mathrm{b}}$	$\omega^{\mathrm{nlt}}_{\mathrm{b}} = \omega^{\mathrm{nlt}}_{\mathrm{dj}} + \omega^{\mathrm{nlt}}_{\mathrm{dk}}$	
Overlapping left triangles ('olt')	j	$\Delta M^{\mathrm{olt}}_{\mathrm{dj}} = C^{\mathrm{olt}}\left[\frac{{w_{\mathrm{jr}}}^{m+2} - {w_{\mathrm{jl}}}^{m+2}}{(m+1)(m+2)} - \frac{h{w_{\mathrm{jl}}}^{m+1}}{m+1}\right]$	$A^{\mathrm{olt}} = \frac{1}{2}h^2$	$\left.\begin{matrix}\left\|\Delta N^{\mathrm{olt}}_{\mathrm{dj}}\right\| \\ \left\|\Delta N^{\mathrm{olt}}_{\mathrm{dk}}\right\| \\ \Delta N^{\mathrm{olt}}_{\mathrm{b}}\end{matrix}\right\} = A^{\mathrm{olt}}C^{\mathrm{olt}}$	$\Delta M^{\mathrm{olt}}_{\mathrm{dj}} = \omega^{\mathrm{olt}}_{\mathrm{dj}}\Delta N^{\mathrm{olt}}_{\mathrm{dk}}$	$\omega^{\mathrm{olt}}_{\mathrm{dj}} = w_{\mathrm{jl}} + \frac{1}{3}h$	
	k	$\Delta M^{\mathrm{olt}}_{\mathrm{dk}} = C^{\mathrm{olt}}\left[\frac{h{u_k}^{m+1}}{m+1} - \frac{{u_k}^{m+2} - {u_{k-1}}^{m+2}}{(m+1)(m+2)}\right]$			$\Delta M^{\mathrm{olt}}_{\mathrm{dk}} = \omega^{\mathrm{olt}}_{\mathrm{dk}}\Delta N^{\mathrm{olt}}_{\mathrm{dk}}$	$\omega^{\mathrm{olt}}_{\mathrm{dk}} = u_k - \frac{1}{3}h$	$C^{\mathrm{olt}} = (n_j^w)^2 \cdot \beta\left(\omega^{\mathrm{olt}}_{\mathrm{dj}}, \omega^{\mathrm{olt}}_{\mathrm{dk}}\right)$
	i	$\Delta M^{\mathrm{olt}}_{m,\mathrm{b}} = \frac{C^{\mathrm{olt}}}{(m+1)(m+2)}\Big[(2w_{\mathrm{jr}})^{m+2} - 2(w_{\mathrm{jl}}+w_{\mathrm{jr}})^{m+2} + (2w_{\mathrm{jl}})^{m+2}\Big]$		$\Delta N^{\mathrm{olt}}_{\mathrm{b}}$	$\Delta M^{\mathrm{olt}}_{\mathrm{b}} = \omega^{\mathrm{olt}}_{\mathrm{b}}\Delta N^{\mathrm{olt}}_{\mathrm{b}}$	$\omega^{\mathrm{olt}}_{\mathrm{b}} = \omega^{\mathrm{olt}}_{\mathrm{dj}} + \omega^{\mathrm{olt}}_{\mathrm{dk}}$	

Notes: $j_\mathrm{p} = [w_{\mathrm{jl}}, w_{\mathrm{jr}}] \in j = [w_{j-1}, w_j]$ $\quad h = w_{\mathrm{jr}} - w_{\mathrm{jl}}$
$k = [u_{k-1} - u_k]$ $\quad h_k = u_k - u_{k-1}$

Table 1: Parameters of four basic geometric shapes in double integral method

$$= \frac{1}{\Delta v_i \bar{v}_i} \left[\left(\frac{d}{dt} \int_{v_{i-1}}^{v_i} n(v) v dv \right) \Big|_{\text{source}} - \left(\frac{d}{dt} \int_{v_{i-1}}^{v_i} n(v) v dv \right) \Big|_{\text{sink}} \right] \tag{19}$$

where $\bar{v}_i$ is the centre of interval i, and

$$\left(\frac{d}{dt} \int_{v_{i-1}}^{v_i} n(v) v dv \right) \Big|_{\text{source}} = \sum_{j \in G_1(i) + G_2(i)} \sum_{\text{loc}} \left[\Delta M_{\text{b}}^{\text{loc}}(i,j) \right] \qquad (\text{loc} = \text{left}, \text{middle}, \text{right}) \tag{20}$$

and

$$\left(\frac{d}{dt} \int_{v_{i-1}}^{v_i} n(v) v dv \right) \Big|_{\text{sink}} = \sum_{p=i}^{i_{\max}} \left[\sum_{j \in [v_{i-1}, v_i]} \sum_{\text{loc}} \Delta M_{\text{dj}}^{\text{loc}}(p,j) + \sum_{k \in [v_{i-1}, v_i]} \sum_{\text{shape}} \Delta M_{\text{dk}}^{\text{shape}}(p, j_{\text{p}}, k) \right] \tag{21}$$

$$(\text{loc} = \text{left}, \text{middle}, \text{right}, \quad \text{shape} = \text{nlt(olt)}, \text{rec}, \text{rt})$$

It must be noted that the determination of the auxiliary grid, geometric factors and volumetric dependence of the kernel are all carried out only once - at the beginning of the simulation - and stored for subsequent use. The operations to be carried out at each time step therefore include only computing products of number densities and updating the kernels for dependence on ambient conditions such as temperature, if needed. This pre-computation greatly enhances the computational efficiency of the method.

3.6 Discretisation of nucleation and growth

The proposed approach will now be combined with a discretisation scheme for nucleation and growth. The former is described by a delta function, while the latter is described by a term involving a first derivative with respect to the particle volume. The starting point is Eq. 22, which we rewrite here as follows:

$$\frac{\partial n}{\partial t} + \frac{\partial (Gn)}{\partial v} = B\delta(v - v_0) + C \tag{22}$$

where C denotes the coagulation terms. By applying the finite volume discretisation, we obtain:

$$\frac{\partial n_i}{\partial t} + \frac{1}{\Delta v_i} \left[n \cdot G(v) \right]_{v_{i-1}}^{v_i} = \frac{1}{\delta v_i} \int_{v_{i-1}}^{v_i} B_i dv_i + C_{\text{d}} \tag{23}$$

where C_{d} denotes the terms resulting from the proposed discretisation method for the coagulation terms. The nucleation rate B_i is non-zero only over the interval including the nuclei volume v_0. For the growth terms, we employ a total variation diminishing (TVD) scheme due to Koren [27], employed before for the PBE by Qamar et al. [43]:

$$[nG(v)]_{v_i} = G(v_i) \left[n_{u(v_i)} + \frac{\phi_i}{2} \left(n_{u(v_i)} - n_{uu(v_i)} \right) \right] \tag{24}$$

where $u(v_i)$ and $uu(v_i)$ are the indices of the two cells upstream of node v_i, and ϕ_i indicates the value of the flux limiter at cell face v_i [43].

4 Testing and validation of the method

4.1 Coagulation kernels

In this section, the method will be tested with a number of canonical problems for the PBE. These include problems with coagulation alone involving various coagulation kernels and initial distributions, as well as a problem of combined coagulation and growth.

The first class of kernels to be tested includes kernels of theoretical importance, due to the fact that they permit analytical solutions of the PBE for coagulation (Eq. 3). These are:

- The constant kernel:

$$\beta(v,w) = \beta_0 \tag{25}$$

- The sum kernel:

$$\beta(v,w) = \beta_0(v+w) \tag{26}$$

- The product kernel:

$$\beta(v,w) = \beta_0 vw \tag{27}$$

The second class includes physically important kernels. As there is no analytical solution for those comparison will be made with direct numerical solutions of the discrete PBE, as will be described in Sec. 4.2. These kernels include:

- The kernel due to collisions of particles in the free-molecular regime:

$$\beta(v,w) = \beta(v,w) = \beta_0 \left(\frac{1}{v} + \frac{1}{w}\right)^{\frac{1}{2}} \left(v^{\frac{1}{3}} + w^{\frac{1}{3}}\right)^2 \tag{28}$$

- The Brownian motion kernel, which governs coagulation of small aerosols:

$$\beta(v,w) = \beta_0 \left(\frac{1}{v^{\frac{1}{3}}} + \frac{1}{w^{\frac{1}{3}}}\right) \left(v^{\frac{1}{3}} + w^{\frac{1}{3}}\right) \tag{29}$$

- The shear kernel, important for coagulation due to laminar shear or turbulent coagulation:

$$\beta(v,w) = \beta_0 \left(v^{\frac{1}{3}} + w^{\frac{1}{3}}\right)^3 \tag{30}$$

Note that, for the physical kernels, the factor β_0 is a function of ambient conditions and hydrodynamic parameters, such as temperature, shear and energy dissipation rate. In the present section, this factor will be set equal to unity, as the focus on testing the method with respect to the volumetric dependence of the kernels. In Sec. 5, where the method will be applied to the simulation of a laminar flame, the full form of the kernels will be employed.

4.2 Direct numerical solution of the discrete PBE

Analytical solutions are available only for a few cases, mainly for the theoretical kernels. To extend the range of test cases to the physically important kernels, comparisons will be made also with direct numerical solutions of the discrete PBE for coagulation, also known as the Smoluchowski equation [60]:

$$\frac{dN_i}{dt} = \frac{1}{2}\sum_{j=1}^{i-1} \beta_{j,i-j} N_j N_{i-j} - N_i \sum_{j=1}^{\infty} \beta_{ij} N_j \tag{31}$$

where N_i is the number density and β_{ij} is the coagulation kernel. The discrete PBE is a closed set of ODEs and can be solved numerically with no approximations other than the error involved in the temporal integration. However, one has to solve for all possible particle sizes, resulting in an extremely large set of ODEs, which makes the solution not useful for practical purposes, although it can serve as a benchmark for

numerical methods. In our test cases, 5000 to 10000 discrete sizes were used, while the temporal integration was carried out with the same method as for the conservative finite volume method (Runge-Kutta 4th order).

For the monodisperse distribution, however, the correspondence between the discrete and continuous PBE is not exact for the first few sizes (0.1-1 in the test cases). A monodisperse distribution in the discrete formulation would correspond to a delta function in the continuous one, but this is not possible to implement; instead one has to distribute the particles over an interval and ensure that the number of particles is consistent. This results in a discrepancy of the two solutions at the initial range, which is of no relevance for the accuracy of the numerical method; a meaningful comparison can be made after size 1.

4.3 Initial distributions and parameters

Two types of the initial distribution will be tested. The first is an exponential initial distribution:

$$n(v,0) = \frac{N_0}{v_0} \mathrm{e}^{-\frac{v}{v_0}} \tag{32}$$

where N_0 is the total number of particles and v_0 is the mean volume in the initial distribution. For simplicity, we set $N_0 = 1$, $v_0 = 1$ on our test cases. The second is a monodisperse distribution:

$$n(v,0) = \begin{cases} 1, v \in (0.1, 0.5) \\ 0, \mathrm{otherwise} \end{cases}$$

The grid employed is exponential in all cases. The remaining parameters are shown in Table 2.

Initial distribution	Kernel $\beta(w,v)$	Size range	Grid number		Time step (s)
			Proposed method	Discrete method	
Exponential $n(v,0) = \frac{N_0}{v_0} \mathrm{e}^{v/v_0}$	constant	0.1-1000	30	analytical solution	0.01
	sum				
	product				
	free-molecular motion			5000	
	Brownian motion				
	shear				
Monodisperse $n(v,0) = \begin{cases} 1, v \in (0.1, 0.5) \\ 0, \mathrm{otherwise} \end{cases}$	constant	0.1-400	30	10000	0.01
	sum				
	product				
	free-molecular motion				
	Brownian motion				
	shear				

Table 2: Parameters for the coagulation test cases

4.4 Convergence study

A convergence study was conducted to determine the minimum number of grid points required for the test cases, by solving the PBE for coagulation with the sum and Brownian kernels, an exponential initial distribution and grids with 30, 40 and 60 nodes (Fig. 7). Converged results can be accomplished with 30 nodes, and therefore this grid was employed in the subsequent tests.

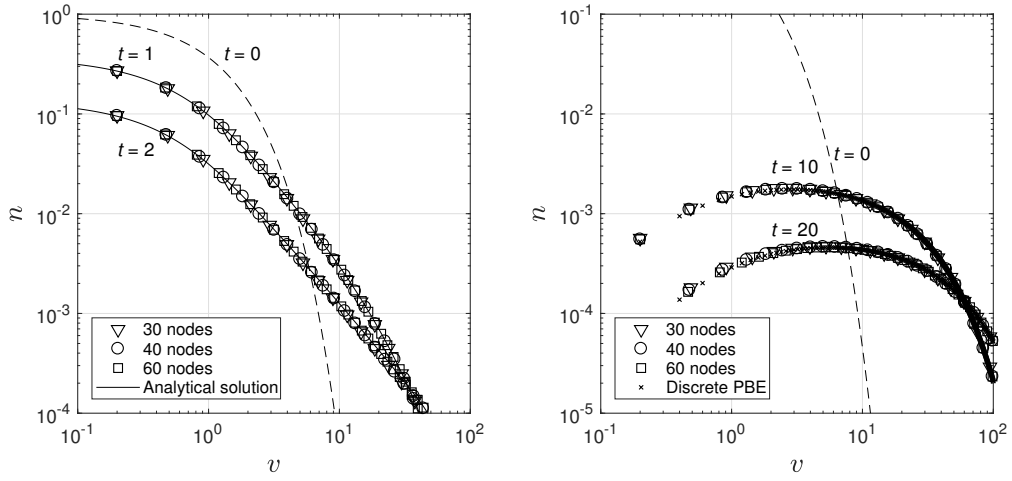

(a) Sum kernel (b) Brownian kernel

Figure 7: Grid convergence test for the coagulation process with an exponential initial distribution

4.5 Exponential initial distribution

Analytical solutions of the coagulation equation have been derived for the constant, sum and product kernels with the exponential initial distribution [35, 54]. Results are shown in Fig. 8 for several time steps. The proposed method exhibits excellent accuracy for all cases. The method can also be adapted to conserve a moment of an arbitrary order, and results are also shown for the conservation of the zeroth and second moment. Best results are obtained with the conservation of the first moment, although all of them are very accurate. The difference is more evident for $v > 10$, where the first moment-based solution is still very accurate, while the others exhibit slight deviations.

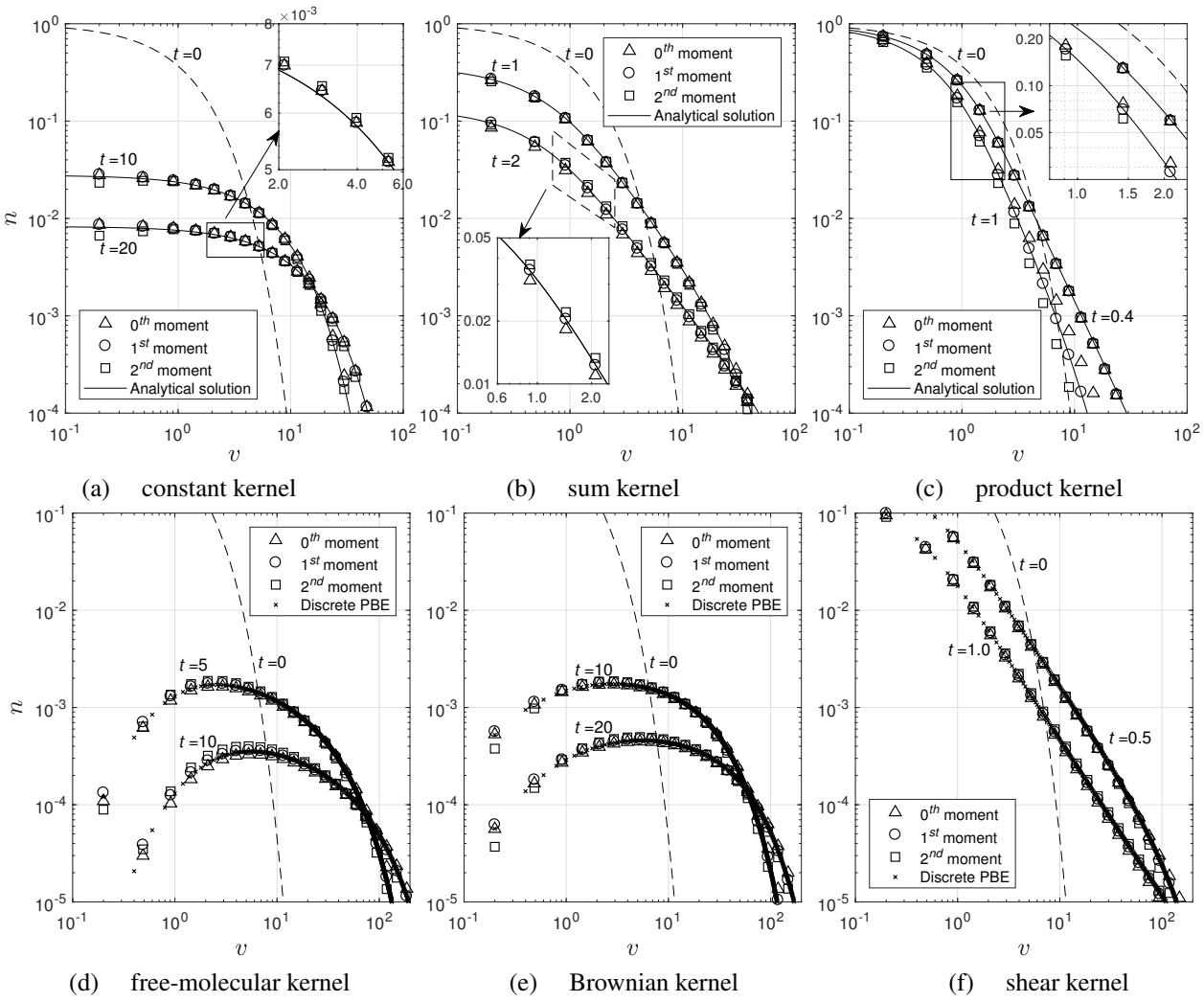

Figure 8: Coagulation process with an exponential initial distribution

4.6 Monodisperse initial distribution

The method will now be tested for a coagulation process with a monodisperse initial distribution, with the same selection of kernels. This case is more physically relevant, as it corresponds to the coagulation of an initially monodisperse population, which is encountered in many real processes. Comparison will be made with solutions of the discrete PBE. Fig. 9 displays logarithmic plots of the distribution. As explained in Sec. 4.2, the implementation of the monodisperse initial distribution is not fully consistent in the two formulations and the comparison is meaningful above size 1. In general, the proposed method conserving the first moment performs very well. Some small deviations appear when the method is set up to conserve the zeroth or the second moment (Fig. 9).

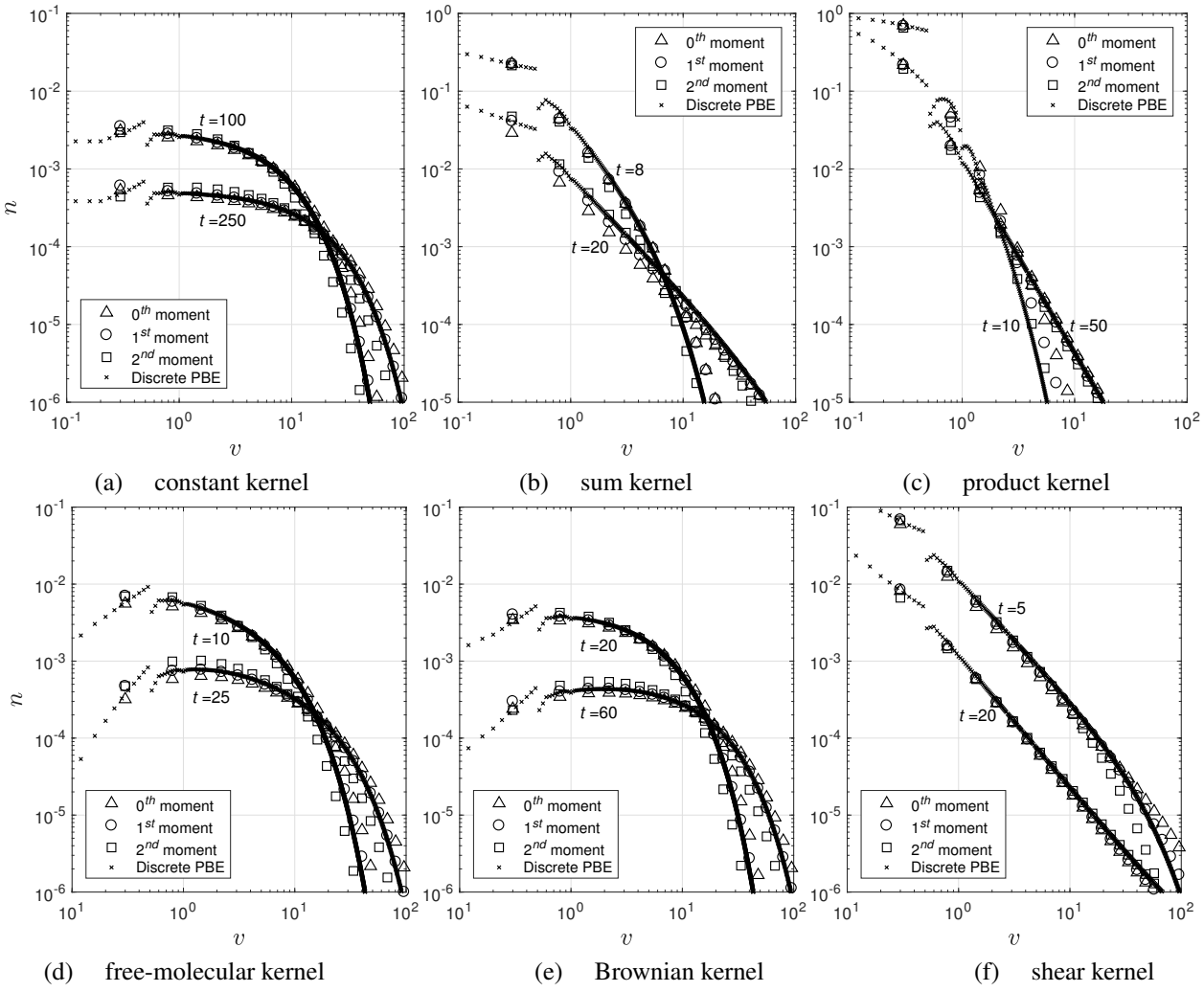

(a) constant kernel (b) sum kernel (c) product kernel

(d) free-molecular kernel (e) Brownian kernel (f) shear kernel

Figure 9: Coagulation process with a monodisperse initial distribution

4.7 Combined coagulation and growth with an exponential initial distribution

This case was studied by Ramabhadran et al. [44], who derived an analytical solution for the constant and sum coagulation kernels and a linear size-dependent growth term ($G = k_{\mathrm{g}} v$), with an exponential initial distribution. In the discretised PBE, the growth term are treated with a total variation diminishing (TVD) method, as described in Sec 3.6. Fig. 10 shows the numerical results by the proposed method with 30 nodes of the PBE grid and the analytical solution ($k_{\mathrm{g}} = 0.1$). The comparison with the analytical solution is again very good.

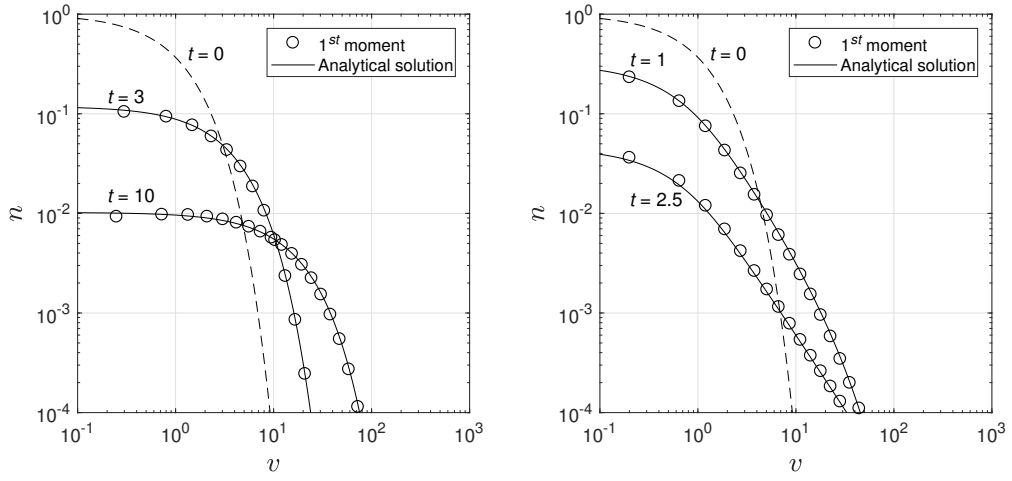

(a) constant kernel (b) sum kernel

Figure 10: Coagulation and growth (size-dependent), comparison of simulation with the analytical solution by Ramabhadran et al. [44]

5 Application to soot formation in a laminar diffusion flame

In this section, the proposed method is coupled with fluid dynamics, chemical kinetics, transport phenomena and radiation, in order to simulate soot formation in a laminar co-flow diffusion flame. This flame has been investigated experimentally by Santoro et al. [52, 53] and numerically in a number of studies (e.g. [11, 1]). The reason for employing the laminar co-flow diffusion flame as our test case is that its simulation requires coupling of the PBE with a full 2D unsteady CFD simulation, as opposed to ideal reactors and 1-D premixed laminar flames that can be computed with 0-D and 1-D codes and assumed temperature profiles. The main objective here is to investigate the numerical performance of the method in the context of a comprehensive unsteady CFD simulation, and in particular to measure the CPU overhead imposed by the proposed method. The study therefore paves the way for the application of the method to turbulent flames and combustors.

5.1 Coupling of PBE and flow

To obtain the spatially inhomogeneous population balance equation, we consider a spatially varying number density, $n(v, \mathbf{x}, t)$, and augment the PBE with terms representing transport in physical space, while the nucleation and growth kinetics are functions of the species concentration vector $\mathbf{Y}(\mathbf{x}, t)$:

$$\begin{aligned} &\frac{\partial n}{\partial t} + \frac{\partial \left[(\mathbf{u} + \mathbf{u}^{\mathrm{t}})n\right]}{\partial x_i} + \frac{\partial \left[G(v, \mathbf{Y})n\right]}{\partial v} \\ &= \dot{B}(\mathbf{Y})\delta(v - v_0) + \frac{1}{2}\int_0^v \beta(v - w, w)n(v - w)n(w)dw - \int_0^\infty \beta(v, w)n(v)n(w)dw \end{aligned} \tag{33}$$

where again the dependence of n and $\mathbf{Y}$ has been omitted where appropriate. In this equation, $\mathbf{u}^{\mathrm{t}}$ represents the thermophoretic velocity of particles [22] and u_i is the gas phase velocity. The function $G(v, \mathbf{Y})$ is the combined surface growth and oxidation rate, while $\dot{B}(\mathbf{Y})$ denotes the nucleation rate.

Eq. 33 must be coupled with the continuity, Navier-Stokes, energy and species transport equations. Numerical solution of the complete system is accomplished by treating the discretised number densities as transported scalars, with the source terms for the PBE provided by the proposed method.

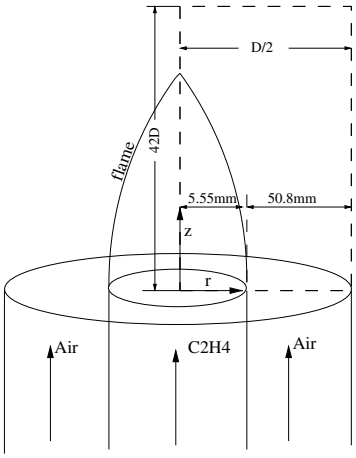

Figure 11: Representation of the computational domain

5.2 Kinetic models

The soot model considers a complete set of processes: nucleation, surface growth and oxidation, PAH surface condensation and particle coagulation. The nucleation step is described by the dimerisation of two PAH species [6], while the HACA mechanism [2] extended with three extra reactions [62] is employed for the growth and oxidation processes. The soot surface growth is also enhanced by the condensation of PAHs, especially in lower temperature regions of a diffusion flame. In order to account for fractal shapes while maintaining a one-dimensional particle property space (volume), soot particles are assumed to be spherical or fractal, depending on their size. Fractal aggregates are assumed to be composed of primary particles with an average primary particle size of $d_{\mathrm{p,a}} = 30.8$ nm, typical of laminar diffusion sooting flames (see e.g. [16]). The number of primary particles in a fractal-like agglomerate can be estimated according to a power law [15]:

$$N_{\mathrm{p}}(v) = \frac{v}{v_{\mathrm{p,a}}} = k_{\mathrm{f}} \left(\frac{d_{\mathrm{g}}(v)}{d_{\mathrm{p,a}}} \right)^{D_{\mathrm{f}}} \tag{34}$$

where v is the volume of the agglomerate, $d_{\mathrm{g}}(v)$ denotes the diameter of gyration, $k_{\mathrm{f}} = 1.94$ is the fractal prefactor [31] and $D_{\mathrm{f}} = 1.8$ is the fractal dimension [8].

Coagulation kernels for the free molecule ($\beta^{\mathrm{fm}}(v,w)$) and the continuum ($\beta^{\mathrm{c}}(v,w)$) regime are employed, described according to [61]:

$$\beta^{\mathrm{fm}}(v,w) = C_{\mathrm{a}} \sqrt{\frac{\pi k_{\mathrm{B}} T}{\rho_{\mathrm{s}}(v+w)}} \left(d(v) + d(w)\right)^2 \tag{35}$$

$$\beta^{\mathrm{c}}(v,w) = \frac{2 k_{\mathrm{B}} T}{3\mu} \left(\frac{C(v)}{d(v)} + \frac{C(w)}{d(w)} \right) \left(d(v) + d(w)\right) \tag{36}$$

where k_{B} denotes Boltzmann's constant, T is the temperature and μ is the viscosity of the fluid. The van der Waals enhancement factor C_{a} with a given value 2.2 [26]. $d(v)$ represents the diameter of a spherical particle or the diameter of gyration of an aggregate. The Cunningham slip correction factor $C(v)$ is a function dependent on Knudsen number of a particle:

$$C(v) = 1 + 1.257\,\mathrm{Kn}(v) \tag{37}$$

The free molecule regime kernel β^{fm} is employed for $\min(\mathrm{Kn}(v), \mathrm{Kn}(w)) > 10$, while the Brownian coagulation kernel is employed for $\max(\mathrm{Kn}(v), \mathrm{Kn}(w)) < 0.1$ (continuum regime). Between these two

regimes, the transition kernel β^{tr} is used [41]:

$$\beta^{\mathrm{tr}}(v,w) = \frac{\beta^{\mathrm{fm}}(v,w)\beta^{\mathrm{c}}(v,w)}{\beta^{\mathrm{fm}}(v,w) + \beta^{\mathrm{c}}(v,w)} \tag{38}$$

As explained in Sec.3.5, the volumetric dependence of the kernels is tabulated. Therefore, only the remaining part needs to be updated at each time step, in order to account for the variation in temperature.

The gas phase chemical kinetics are described by the ABF mechanism [2], which includes 101 species and 574 chemical reactions. Finally, a radiation model based on the assumption of optical thinness [20, 21] is employed.

5.3 Test case and simulation setup

The co-flow diffusion burner (Santoro burner) [52] consists of an $11.1\,\mathrm{mm}$ ID nozzle protruding $4\,\mathrm{mm}$ above a $101.6\,\mathrm{mm}$ diameter co-flow, and is shown schematically in Fig. 11. The simulation is carried out with the in-house CFD code BOFFIN. The spatial grid includes 200 and 100 cells in the axial and radial directions respectively, and is refined towards the jet exit and the interface between the fuel and air streams. A uniform velocity profile is set at the inlet, while ambient pressure is assumed at the outlet. A symmetry boundary condition is applied along the flame centreline, while the velocity at the edge of the domain around the flame is set equal to the input velocity of the air channel.

5.4 Results

Fig. 12 compares the measured values of the integrated soot volume fraction (ISVF) [52] on each cross-section above from the nozzle exit plane with the predictions by the coupled CFD-PBE simulation. A convergent result is achieved by the PBE with 60 PBE grid nodes, while the solution with 40 nodes exhibits an underprediction. The comparison with the experimental results for the integrated soot volume fraction is quite good.

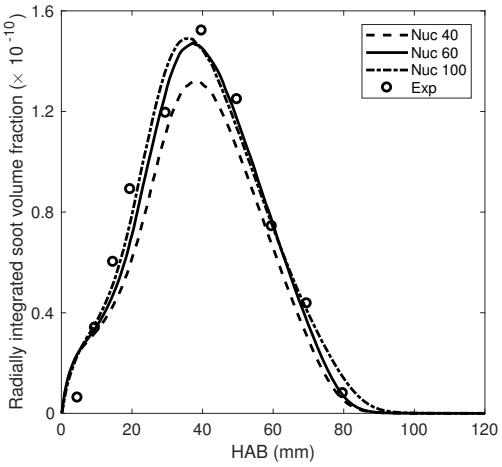

Figure 12: Integrated soot volume fraction at different heights above burner, predictions with different PBE grids

Fig.13 shows comparisons of the predicted temperature profiles with the measured data of Santoro [52] at several heights and at the centreline of the flame. The predicted temperature is about 50-100 K lower than the measured data around the flame centre at 20-30 mm height above the burner, while it is about 50 K higher downstream at 50 mm height. However, the temperature profiles are overall well predicted at the two wings of the flames, around 3 mm or further away from the centreline. Finally, Fig. 14 shows the spatial

evolution of the particle size distributions on the axial line of 3 mm parallel to the centreline, where the soot production is maximum. A bimodal distribution begins to form at a height of 10 mm and is evident at 30 mm height above the burner.

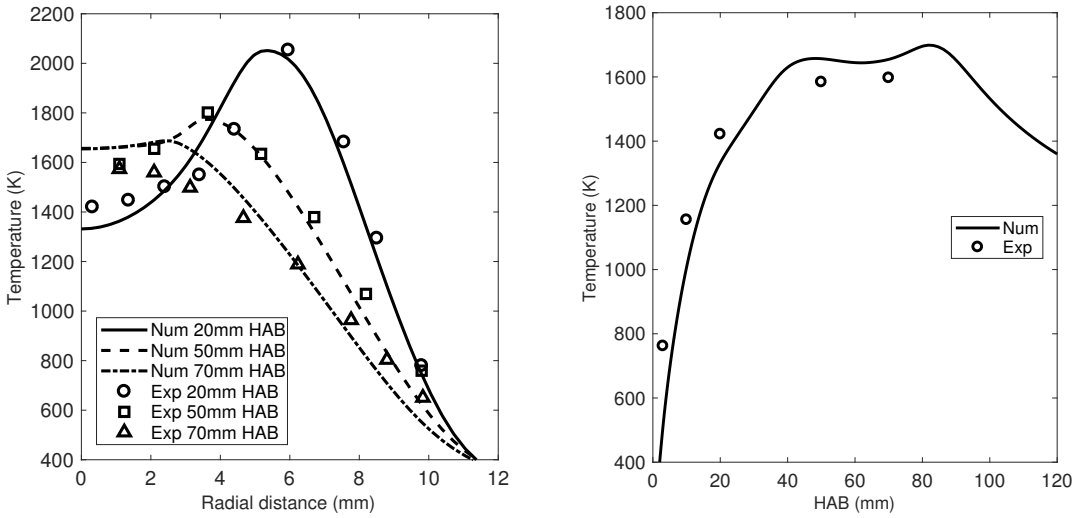

(a) Radial profiles of temperature at various cross-sections

(b) The temperature profile on the centreline

Figure 13: Comparisons of temperature profiles at different height above the burner and on the centreline

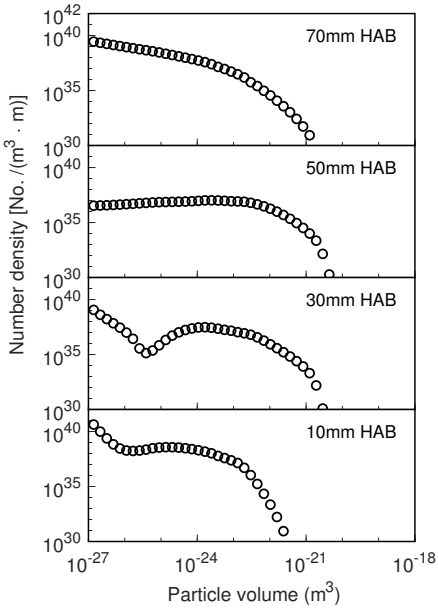

Figure 14: Particle size distribution at different heights on the axial line 3mm away from the centerline

Table 3 shows a breakdown of the CPU time spent in different parts of the code for three different PBE grids. The part spent in the PBE solution occupies only 5.0% of the total CPU time when 40 PBE nodes are employed, which increases to 8.2% with 60 PBE nodes and to 14.2% with 100 nodes. The number of operations in the growth term is proportional to the number of PBE grid nodes, while for the coagulation term it is proportional to the square of the number of nodes. Therefore, the coagulation process is the most

Subroutines		Time consumption (%)		
		40 nodes	60 nodes	100 nodes
Flow field		19.5	15.5	11.1
Scalar convection & diffusion		29.5	40.0	51.2
Chemistry		46.0	36.3	23.5
PBE (total)		5.0	8.2	14.2
Breakdown of PBE step:				
	nucleation & growth	0.8	0.8	0.7
	coagulation algorithm	1.6	2.8	5.1
	coagulation kernel	2.6	4.6	8.4

Table 3: CPU time breakdown for the various parts of the coupled CFD-PBE simulation (average over 200 time steps).

time-consuming part of the PBE calculation. Furthermore, more than 50% of the computational cost for the PBE (in the 60-node case) is consumed for updating the coagulation kernel to account for its dependence on the ambient conditions. The proportion of the time spent on the PBE discretisation is therefore very modest, and it can be concluded that the proposed method provides an efficient means for coupling the PBE with CFD.

6 Conclusions

In this paper, we presented a conservative finite volume method for the discretisation of the PBE with nucleation, growth and coagulation. The main innovation of the method lies in the discretisation scheme for coagulation, which attains accurate prediction of the distribution while conserving the first moment (or any other single moment) and employing a small number of PBE nodes (or sections). Furthermore, the method is applicable to an arbitrary non-uniform grid and could also be combined with an adaptive grid approach, such as the one developed in [56].

The main elements of the method are: a) the employment of an auxiliary grid of complementary points that are needed to accurately calculate all coagulation events, b) a geometric approach to the evaluation of the double integrals resulting from the finite volume integration of the coagulation terms, and c) the detailed balancing of source and sink terms to ensure moment conservation. The auxiliary grid, geometric factors and volumetric dependence of the kernels are all pre-calculated and stored, and thus do not affect the computational efficiency of the method. Extensive testing of the method with analytical solutions and direct numerical solutions of the discrete PBE was carried out with both theoretical and physically realistic kernels. Results showed that the method produces very accurate solutions that conserve the chosen moment, even on coarse grids.

The ultimate objective of this work is to propose a method that is robust and economic to allow for the solution of the discretised PBE when coupled with flow, and thus enable the modelling of problems such as soot formation in flames. To test the method in this context, a laminar co-flow diffusion sooting flame was simulated, for which the PBE solver had to be coupled with a CFD solver, chemical kinetics, transport and radiation models. Good agreement with experimental results was obtained, and furthermore two important conclusions can be drawn from this case. First, a relatively coarse grid comprising 60 nodes was sufficient, and second, the computational effort required to solve the discretised PBE was only 8.2% of the time taken for the complete simulation. These facts indicate that the discretisation method is both accurate and economic, and therefore suitable for coupling with comprehensive CFD simulations. Future work will explore the application of the method to turbulent flows with soot formation.

Acknowledgements

Anxiong Liu would like to acknowledge the financial support from the Chinese Scholarship Council (CSC).

References

[1] P. Akridis and S. Rigopoulos. Modelling of soot formation in laminar diffusion flames using a comprehensive cfd-pbe model with detailed gas-phase chemistry. *Combustion Theory and Modelling*, 21 (1):35–48, 2017.

[2] J. Appel, H. Bockhorn, and M. Frenklach. Kinetic modeling of soot formation with detailed chemistry and physics: Laminar premixed flames of C2 hydrocarbons. *Combustion and Flame*, 121(1-2):121–136, 2000.

[3] D. Aubagnac-Karkar, J.-B. Michel, O. Colin, P. E. Vervisch-Kljakic, and N. Darabiha. Sectional soot model coupled to tabulated chemistry for diesel RANS simulations. *Combustion and Flame*, 162(8): 3081–3099, 2015.

[4] D. Aubagnac-Karkar, A. El Bakali, and P. Desgroux. Soot particles inception and PAH condensation modelling applied in a soot model utilizing a sectional method. *Combustion and Flame*, 189:190–206, 2018.

[5] M. Balthasar and M. Kraft. A stochastic approach to calculate the particle size distribution function of soot particles in laminar premixed flames. *Combustion and Flame*, 133(3):289–298, 2003.

[6] G. Blanquart and H. Pitsch. A joint volume-surface-hydrogen multi-variate model for soot formation. In H. Bockhorn, A. D'Anna, A. F. Sarofim, and H. Wang, editors, *Combustion Generated Fine Carbonaceous Particles*, pages 437–463. KIT Scientific Publishing, Karlsruhe, 2009.

[7] R. Bleck. A fast, approximative method for integrating the stochastic coalescence equation. *Journal of Geophysical Research*, 75(27):5165–5171, 1970.

[8] A. M. Brasil, T. L. Farias, and M. G. Carvalho. A recipe for image characterization of fractal-like aggregates. *Journal of Aerosol Science*, 30(10):1379–1389, 1999.

[9] M. B. Colket and R. J. Hall. Successes and uncertainties in modelling soot formation in laminar, premixed flames. In H. Bockhorn, editor, *Soot Formation in Combustion, Springer Series in Chemical Physics 59*, pages 442–470. Springer-Verlag, 1994.

[10] R. Drake. A general mathematical survey of the coagulation equation. In G. M. Hidy and J. R. Brock, editors, *Topics in Current Aerosol Research*, pages 204–376. Pergamon, 1972.

[11] S.B. Dworkin, Q. Zhang, M.J. Thomson, N.A. Slavinskaya, and U. Riedel. Application of an enhanced pah growth model to soot formation in a laminar coflow ethylene/air diffusion flame. *Combustion and Flame*, 158(9):1682–1695, 2011.

[12] F. Filbet and P. Laurençot. Numerical simulation of the smoluchowski coagulation equation. *SIAM Journal on Scientific Computing*, 25(6):2004–2028, 2004.

[13] M. Frenklach and S.J. Harris. Aerosol dynamics modeling using the method of moments. *Journal of Colloid And Interface Science*, 118(1):252–261, 1987.

[14] S. K. Friedlander. *Smoke, Dust, and Haze: Fundamentals of Aerosol Dynamics*. Oxford University Press, 2 edition, 2000.

[15] S. K. Friedlander. *Smoke, Dust and Haze*. Oxford University Press, Oxford, New York, second edition, 2000.

[16] Carlos E. Garcia Gonzalez. *Characterization of nanoparticles generated in reacting flows*. PhD thesis, Imperial College London, 2018.

[17] F. Gelbard and J. H. Seinfeld. Numerical solution of the dynamic equation for particulate systems. *Journal of Computational Physics*, 28(3):357–375, 1978.

[18] F. Gelbard and J. H. Seinfeld. Simulation of multicomponent aerosol dynamics. *Journal of Colloid and Interface Science*, 78(2):485–501, 1980.

[19] F. Gelbard, Y. Tambour, and J. H. Seinfeld. Sectional representations for simulating aerosol dynamics. *Journal of Colloid and Interface Science*, 76(2):541–556, 1980.

[20] R. J. Hall. The radiative source term for plane-parallel layers of reacting combustion gases. *Journal of Quantitative Spectroscopy and Radiative Transfer*, 49(5):517–523, 1993.

[21] R. J. Hall. Radiative dissipation in planar gas-soot mixtures. *Journal of Quantitative Spectroscopy and Radiative Transfer*, 51(4):635–644, 1994.

[22] R. J. Hall, M. D. Smooke, and M. B. Colket. Predictions of soot dynamics in opposed jet diffusion flames. In F. K. Dryer and R. F. Sawyer, editors, *Physical and Chemical Aspects of Combustion: A Tribute to Irvin Glassman*, pages 189–229. CRC Press, 1997.

[23] M. J. Hounslow, R. L. Ryall, and V. R. Marshall. A discretized population balance for nucleation, growth, and aggregation. *AIChE Journal*, 34(11):1821–1832, 1988.

[24] H.M. Hulburt and T. Akiyama. Liouville equations for agglomeration and dispersion processes. *Industrial and Engineering Chemistry Fundamentals*, 8(2):319–324, 1969.

[25] H.M. Hulburt and S. Katz. Some problems in particle technology. a statistical mechanical formulation. *Chemical Engineering Science*, 19(8):555–574, 1964.

[26] A. Kazakov and M. Frenklach. Dynamic modeling of soot particle coagulation and aggregation: Implementation with the method of moments and application to high-pressure laminar premixed flames. *Combustion and Flame*, 114(3-4):484–501, 1998.

[27] B. Koren. Numerical methods for advection - diffusion problems. In *Notes on Numerical Fluid Mechanics and Multidisciplinary Design*, volume 45, pages 117–138. Vieweg Verlag, 1993.

[28] S. Kumar and D. Ramkrishna. On the solution of population balance equations by discretization - i. a fixed pivot technique. *Chemical Engineering Science*, 51(8):1311–1332, 1996.

[29] S. Kumar and D. Ramkrishna. On the solution of population balance equations by discretization - ii. a moving pivot technique. *Chemical Engineering Science*, 51(8):1333–1342, 1996.

[30] F. Laurent, A. Sibra, and F. Doisneau. Two-size moment multi-fluid model: A robust and high-fidelity description of polydisperse moderately dense evaporating sprays. *Communications in Computational Physics*, 20(4):902–943, 2016.

[31] O. Link, D.R. Snelling, Thomson K.A., and G.J. Smallwood. Development of absolute intensity multi-angle light scattering for the determination of polydisperse soot aggregate properties. *Proceedings of the Combustion Institute*, 33(1):4848–4854, 2011.

[32] P. Marchal, R. David, J. P. Klein, and J. Villermaux. Crystallization and precipitation engineering - i. an efficient method for solving population balance in crystallization with agglomeration. *Chemical Engineering Science*, 43(1):59–67, 1988.

[33] D. L. Marchisio and R. O. Fox. Solution of population balance equations using the direct quadrature method of moments. *Journal of Aerosol Science*, 36(1):43–73, 2005.

[34] R. McGraw. Description of aerosol dynamics by the quadrature method of moments. *Aerosol Science and Technology*, 27(2):255–265, 1997.

[35] Z. A. Melazak. The effect of coalescence in certain collision processes. *Quarterly of Applied Mathematics*, 11:231–234, 1953.

[36] M. E. Mueller, G. Blanquart, and H. Pitsch. Hybrid method of moments for modeling soot formation and growth. *Combustion and Flame*, 156(6):1143–1155, 2009.

[37] K. Netzell, H. Lehtiniemi, and F. Mauss. Calculating the soot particle size distribution function in turbulent diffusion flames using a sectional method. *Proceedings of the Combustion Institute*, 31(1): 667–674, 2007.

[38] T.T. Nguyen, F. Laurent, R.O. Fox, and M. Massot. Solution of population balance equations in applications with fine particles: Mathematical modeling and numerical schemes. *Journal of Computational Physics*, 325:129–156, 2016.

[39] M. Nicmanis and M. J. Hounslow. Finite-element methods for steady-state population balance equations. *AIChE Journal*, 44(10):2258–2272, 1998.

[40] C. J. Pope and J. B. Howard. Simultaneous particle and molecule modeling (SPAMM): An approach for combining sectional aerosol equations and elementary gas-phase reactions. *Aerosol Science and Technology*, 27(1):73–94, 1997.

[41] S.E. Pratsinis. Simultaneous nucleation, condensation, and coagulation in aerosol reactors. *Journal of Colloid And Interface Science*, 124(2):416–427, 1988.

[42] S. Qamar and G. Warnecke. Solving population balance equations for two-component aggregation by a finite volume scheme. *Chemical Engineering Science*, 62(3):679–693, 2007.

[43] S. Qamar, M. P. Elsner, I. A. Angelov, G. Warnecke, and Seidel-Morgenstern. A. A comparative study of high resolution schemes for solving population balances in crystallization. *Computers and Chemical Engineering*, 30(6):1119–1131, 2006.

[44] T. E. Ramabhadran, T. W. Peterson, and J. H. Seinfeld. Dynamics of aerosol coagulation and condensation. *AIChE journal*, 22(5):840–851, 1976.

[45] D. Ramkrishna. *Population Balances: Theory and Applications to Particulate Systems in Engineering*. Academic Press, 2000.

[46] H. Richter, S. Granata, W. H. Green, and J. B. Howard. Detailed modeling of PAH and soot formation in a laminar premixed benzene/oxygen/argon low-pressure flame. *Proceedings of the Combustion Institute*, 30(1):1397–1405, 2005.

[47] S. Rigopoulos. Population balance modelling of polydispersed particles in reactive flows. *Progress in Energy and Combustion Science*, 36(4):412–443, 2010.

[48] S. Rigopoulos and A. G. Jones. Finite-element scheme for solution of the dynamic population balance equation. *AIChE Journal*, 49(5):1127–1139, 2003.

[49] P. Rodrigues, B. Franzelli, R. Vicquelin, O. Gicquel, and N. Darabiha. Unsteady dynamics of PAH and soot particles in laminar counterflow diffusion flames. *Proceedings of the Combustion Institute*, 36(1):927–934, 2017.

[50] P. Rodrigues, B. Franzelli, R. Vicquelin, O. Gicquel, and N. Darabiha. Coupling an LES approach and a soot sectional model for the study of sooting turbulent non-premixed flames. *Combustion and Flame*, 190:477–499, 2018.

[51] A. I. Roussos, A. H. Alexopoulos, and C. Kiparissides. Part iii: Dynamic evolution of the particle size distribution in batch and continuous particulate processes: A Galerkin on finite elements approach. *Chemical Engineering Science*, 60(24):6998–7010, 2005.

[52] R. J. Santoro, H. G. Semerjian, and R. A. Dobbins. Soot particle measurements in diffusion flames. *Combustion and Flame*, 51:203–218, 1983.

[53] R. J. Santoro, T. T. Yeh, J. J. Horvath, and H. G. Semerjian. The transport and growth of soot particles in laminar diffusion flames. *Combustion Science and Technology*, 53:89–115, 1987.

[54] W. T. Scott. Analytical studies of cloud droplet coalescence i. *Journal of the Atomspheric Sciences*, 25:54–65, 1968.

[55] F. Sewerin and S. Rigopoulos. Algorithmic aspects of the les-pbe-pdf method for modeling soot particle size distributions in turbulent flames. *Combustion Science and Technology, in press*.

[56] F. Sewerin and S. Rigopoulos. An explicit adaptive grid approach for the numerical solution of the population balance equation. *Chemical Engineering Science*, 168:250–270, 2017.

[57] F. Sewerin and S. Rigopoulos. An les-pbe-pdf approach for modeling particle formation in turbulent reacting flows. *Physics of Fluids*, 29(10), 2017.

[58] F. Sewerin and S. Rigopoulos. An les-pbe-pdf approach for predicting the soot particle size distribution in turbulent flames. *Combustion and Flame*, 189:62–76, 2018.

[59] J.A. Shohat and J.D. Tamarkin. *The problem of moments*. American Mathematical Society, 1943.

[60] M. V. Smoluchowski. Mathematical theory of the kinetics of coagulation of colloidal systems. *Z. Phys. Chem.*, pages 129–168, 1917. ISSN 92.

[61] S. Vemury and S.E. Pratsinis. Self-preserving size distributions of agglomerates. *Journal of Aerosol Science*, 26(2):175–185, 1995.

[62] Y. Wang, A. Raj, and S. H. Chung. Soot modeling of counterflow diffusion flames of ethylene-based binary mixture fuels. *Combustion and Flame*, 162(3):586–596, 2015.

[63] E.R. Whitby and P.H. McMurry. Modal aerosol dynamics modeling. *Aerosol Science and Technology*, 27(6):673–688, 1997.

[64] M. Williams and S. Loyalka. *Aerosol Science - Theory and Practice: With Special Applications to the Nuclear Industry*. Pergamon Press, Oxford, 1991.

[65] M.M.R. Williams. Some topics in nuclear aerosol dynamics. *Progress in Nuclear Energy*, 17(1):1–52, 1986.

[66] D.L. Wright Jr. Numerical advection of moments of the particle size distribution in eulerian models. *Journal of Aerosol Science*, 38(3):352–369, 2007.

[67] S. Yang and M.E. Mueller. A multi-moment sectional method (mmsm) for tracking the soot number density function. *Proceedings of the Combustion Institute*, 2018.